JCI insight

Inhibiting neddylation modification alters mitochondrial morphology and reprograms energy metabolism in cancer cells

Qiyin Zhou,[1,2] Hua Li,[3] Yuanyuan Li,[1] Mingjia Tan,[3] Shaohua Fan,[3] Cong Cao,[4] Feilong Meng,[4] Ling Zhu,[4] Lili Zhao,[5] Min-Xin Guan,[4] Hongchuan Jin,[2] and Yi Sun[1,3]

[1]Cancer Institute of the Second Affiliated Hospital and Institute of Translational Medicine, Zhejiang University School of Medicine, Hangzhou, Zhejiang, China. [2]Laboratory of Cancer Biology, Key Lab of Biotherapy in Zhejiang, Sir RunRun Shaw Hospital, Zhejiang University School of Medicine, Hangzhou, Zhejiang, China. [3]Division of Radiation and Cancer Biology, Department of Radiation Oncology, University of Michigan, Ann Arbor, Michigan, USA. [4]Institute of Genetics, Department of Genetics, Zhejiang University School of Medicine, Hangzhou, Zhejiang, China. [5]Department of Biostatistics, University of Michigan, Ann Arbor, Michigan, USA.

Abnormal activation of neddylation modification and dysregulated energy metabolism are frequently seen in many types of cancer cells. Whether and how neddylation modification affects cellular metabolism remains largely unknown. Here, we showed that MLN4924, a small-molecule inhibitor of neddylation modification, induces mitochondrial fission-to-fusion conversion in breast cancer cells via inhibiting ubiquitylation and degradation of fusion-promoting protein mitofusin 1 (MFN1) by SCF$^{\beta\text{-TrCP}}$ E3 ligase and blocking the mitochondrial translocation of fusion-inhibiting protein DRP1. Importantly, MLN4924-induced mitochondrial fusion is independent of cell cycle progression, but confers cellular survival. Mass-spectrometry-based metabolic profiling and mitochondrial functional assays reveal that MLN4924 inhibits the TCA cycle but promotes mitochondrial OXPHOS. MLN4924 also increases glycolysis by activating PKM2 via promoting its tetramerization. Biologically, MLN4924 coupled with the OXPHOS inhibitor metformin, or the glycolysis inhibitor shikonin, significantly inhibits cancer cell growth both in vitro and in vivo. Together, our study links neddylation modification and energy metabolism, and provides sound strategies for effective combined cancer therapies.

Introduction

Energy is the primary limiting factor for growth and reproduction of all biological systems and it is mainly funneled through the mitochondrial oxidative phosphorylation system (OXPHOS) and glycolysis (1). Cancer cells are capable of reprogramming their energy metabolism to adapt to changes in energetic demands (2). Thus, metabolic reprogramming is a hallmark of cancer that supports abnormal growth and survival of malignant cells with sufficient levels of energy and building blocks (3, 4). A better understanding of cancer energy metabolism would have significant implications for cancer pathophysiology and for potential therapeutic interventions (5, 6).

Mitochondria are essential hubs of bioenergetics (7). Moreover, as highly dynamic organelles, mitochondria constantly change their morphology between elongated interconnected networks and fragmented shapes by fusion and fission, depending on their physiological and cellular conditions (8). The fine-tuned mitochondrial fusion and fission dynamics are crucial to maintain mitochondrial function and cellular metabolic reprogramming (9). Consequently, dysregulated mitochondrial dynamics, particularly a switch towards fission status that causes excess mitochondrial fragmentation, contribute to tumorigenesis (10). In addition, many cancer cells favor energy production through a high rate of aerobic glycolysis by enhancing glucose consumption, also known as the Warburg effect (11). The increased glycolysis enables cancer cells to suppress apoptotic signaling and drives their growth and proliferation (12). Pyruvate kinase (PK) catalyzes the last irreversible step in glycolysis and mediates the conversion of phosphoenolpyruvate (PEP) to pyruvate, thus affecting the glycolytic rate. The M2 isoform of pyruvate kinase (PKM2), one splice variant encoded by the *PKM* gene, is the major form of PK in cancer cells and has been found to

Conflict of interest: The authors have declared that no conflict of interest exists.

Submitted: April 11, 2018
Accepted: January 16, 2019
Published: January 22, 2019

Reference information: *JCI Insight*. 2019;4(4):e121582. https://doi.org/10.1172/jci.insight.121582.

play an important role in the Warburg effect (12, 13). Recently, accumulating evidence suggests that oncogenes and tumor suppressor genes in cancer-driving pathways reprogram energy metabolism via mediating mitochondrial dynamics or PKM2 activity (10, 14).

Protein neddylation, one type of posttranslational modification that regulates protein function and stabilization, is catalyzed by an E1 NEDD8-activating enzyme (NAE), one of two E2 neddylation conjugation enzymes, and one of several E3 neddylation ligases (15). Cullin family proteins, the scaffold component of cullin-RING ligase (CRL), have been characterized as physiological substrates of neddylation. Neddylation of cullin activates CRLs, the largest family of E3 ubiquitin ligases, which are responsible for the degradation of approximately 20% of cellular proteins, thereby temporally and precisely regulating many biological processes (15). To date, CRL1, also known as SCF (SKP1-cullin 1-F-box protein), is the best-studied member of the CRLs (16). SCF E3 ligase consists of adaptor protein SKP1, cullin 1, RING protein RBX1, and F-box receptor protein, which determines the substrate specificity (16). β-TrCP (β-transducin repeat–containing protein), one of the best-characterized F-box proteins, regulates many cellular processes by targeting diverse substrates (17).

Accumulated experimental data have clearly demonstrated that the process of protein neddylation modification is overactivated in many human cancers (15). MLN4924, also known as pevonedistat, is the first-in-class inhibitor of NAE, thus inhibiting the entire neddylation modification (18). Numerous in vitro and in vivo preclinical studies have shown that MLN4924 has attractive suppressive activity against a variety of human cancer cells (15, 18). Reported mechanisms of MLN4924 anticancer action include triggering the DNA-damage response, nonhomologous end-joining repair, DNA re-replication stress, and oxidative stress at the biochemical level; and inducing cell cycle arrest, apoptosis, autophagy, and senescence at the cellular level (18–20). To date, whether and how neddylation modification regulates energy metabolism remain largely unknown, although several studies have shown that blockage of neddylation disrupts nucleotide metabolism and affects mitochondrial function through oxidative stress in human acute myeloid leukemia and ovarian cancer cells (21–23).

Here, we show that energy metabolism is largely altered after neddylation blockage by MLN4924. Specifically, MLN4924 caused accumulation of MFN1 via inhibiting its ubiquitylation and degradation by $\text{SCF}^{\beta\text{-TrCP}}$ E3 ligase, and blocked mitochondrial translocation of DRP1 to induce mitochondrial fission-to-fusion conversion. MLN4924 also impaired mitochondrial functions, but increased OXPHOS. In addition, MLN4924 promoted cellular glycolysis by activating PKM2 via inducing its tetramerization. Biologically, combination of MLN4924 with the clinically used OXPHOS inhibitor metformin, or the glycolytic inhibitor shikonin, significantly enhanced killing of breast cancer cells in both in vitro culture models and 2 in vivo xenograft tumor models. This is the first report, to the best of our knowledge, demonstrating mechanistically how neddylation modification regulates energy metabolism. Our study also has translational value by providing a sound rationale for future clinical combination of MLN4924 with inhibitors of OXPHOS or glycolysis to enhance efficacy of cancer therapy.

Results

Blockage of neddylation induces mitochondrial fission-to-fusion conversion. We and the others have previously shown that MLN4924 could trigger oxidative stress (21, 22). Given that the mitochondrion is the major subcellular organelle that regulates cellular oxidation, we examined potential effects of MLN4924 on mitochondrial dynamics. We first transfected 2 breast cancer cell lines, MDA-MB-231 and SK-BR-3, with mito-DS-Red to monitor mitochondrial morphology (24). Mitochondria in vehicle control cells were fragmented with a spherical appearance. Remarkably, following the exposure to MLN4924, mitochondria became a tubular or filament-like network (Figure 1, A and B). The percentage of cells with filamentous mitochondria was significantly increased upon MLN4924 exposure in time- and dose-dependent manners (Figure 1, C and D). We further confirmed this observation using MitoTracker Red staining. Again, MLN4924 altered mitochondrial shape by converting fragmented spheres to interconnected filaments (Supplemental Figure 1, A and B; supplemental material available online with this article; https://doi.org/10.1172/jci.insight.121582DS1). Similar morphological changes induced by MLN4924 were also observed in human bronchial epithelial BEAS2B cells and lung adenocarcinoma A549 cells (Supplemental Figure 1, C and D), indicating a general effect, not cell-line specificity. Finally, to confirm that MLN4924-induced mitochondrial fusion was not due to mitochondrial self-association or aggregation, ultrastructural analysis was performed by electron microscopy. Following MLN4924 treatment, mitochondria changed from a fissional, spherical appearance to an elongated, tubular, fusional shape (Figure 1E).

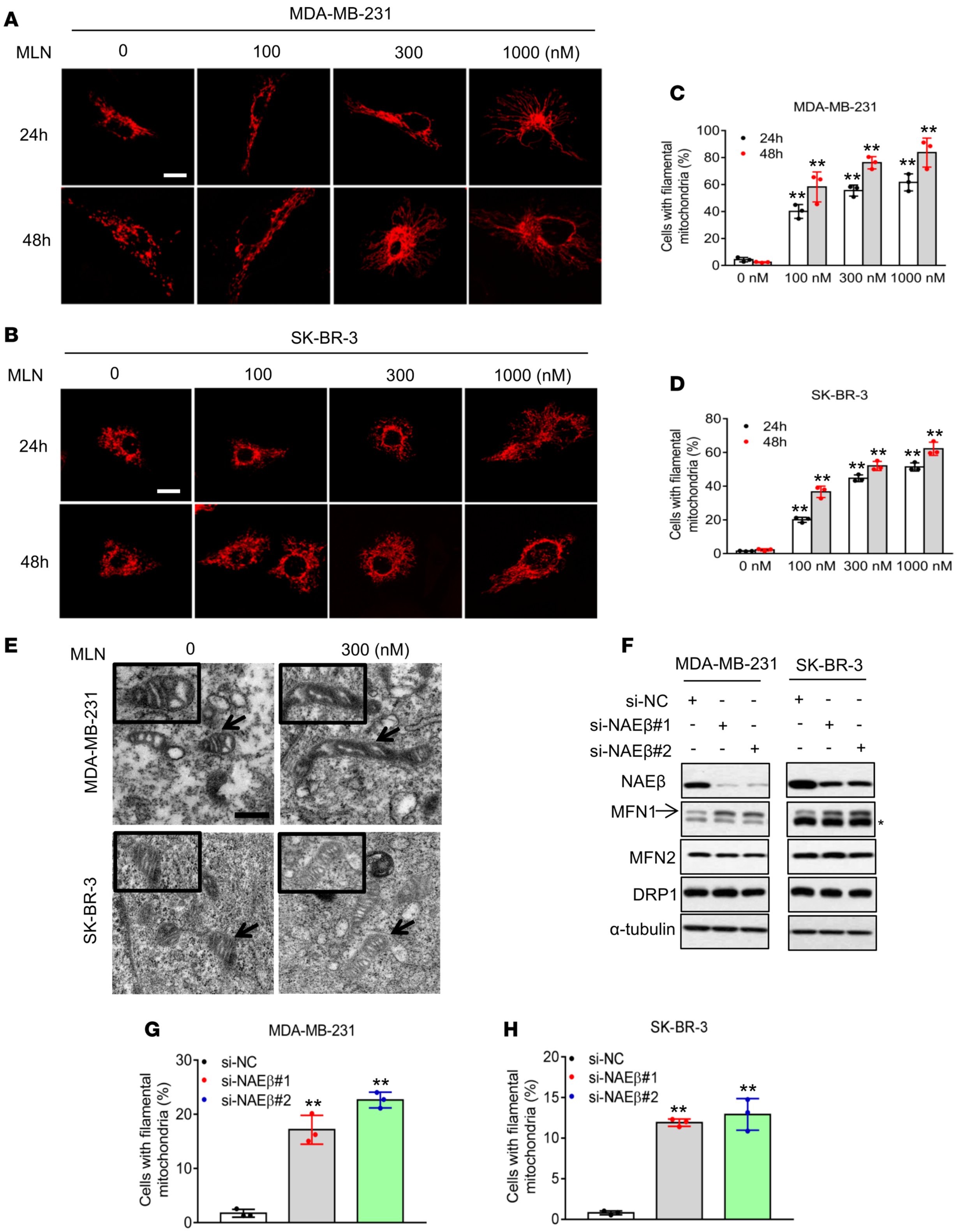

Figure 1. Inhibition of neddylation induces mitochondrial fusion. (**A** and **B**) MDA-MB-231 and SK-BR-3 cells were transfected with Mito-DS-Red and then treated with indicated concentrations of MLN4924 for 24 and 48 hours. The images of mitochondrial morphology were obtained by confocal microscopy. Scale bars: 10 μm. (**C** and **D**) Quantification of the interconnected filamentous mitochondria shown in **A** and **B**, respectively (mean ± SD, *n* = 3). (**E**) MDA-MB-231 and SK-BR-3 cells were treated with 300 nM MLN4924 for 24 hours and fixed for electron microscopy analysis. Scale bars: 0.5 μm. (**F**–**H**) MDA-MB-231 and SK-BR-3 cells were transfected with either scrambled control siRNA (si-NC), or 2 independent siRNAs targeting NAEβ (si-NAEβ-1, si-NAEβ-2) for 48 hours. Cells were then analyzed by Western blotting (**F**) or stained with MitoTracker Red. The asterisk indicates nonspecific bands. Mitochondrial morphology was photographed by confocal microscopy, and the interconnected filamentous mitochondria were quantified. Results were plotted and shown as mean ± SD (*n* = 3) (**G** and **H**). *$P < 0.05$, **$P < 0.01$ by 1-way ANOVA.

To exclude potential off-target effects of MLN4924 on mitochondrial dynamics, we used an siRNA-based approach to knock down NAEβ (Figure 1F), the catalytic subunit of NAE (25), to which MLN4924 binds and inhibits activity (18, 26). NAEβ knockdown also significantly induced filamentous mitochondria in cells (Figure 1, G and H, and Supplemental Figure 1E), indicating that MLN4924-induced mitochondrial fusion happens via inhibiting NAEβ, not an off-target effect. Taken together, our results show that targeting protein neddylation, via either a pharmacological or genetic approach, causes changes in mitochondrial morphology from fragmented spheres to an elongated network through inducing a mitochondrial fission-to-fusion dynamic switch. Given that MLN4924 and siNAEβ have the same effect, with the former being more efficacious, we used MLN4924 for the remainder of our experiments.

MLN4924 alters the levels and localization of mitochondrial dynamic regulators. Elongated mitochondrial morphology might be due to increased fusion, decreased fission, or both. To establish a direct link between MLN4924 and mitochondrial fusion, we determined whether MLN4924 affects the expression of the key regulatory components of mitochondrial dynamics, MFN1, MFN2, and DRP1. We first confirmed that MLN4924 indeed completely inhibited cullin neddylation (Figure 2, A and B, and Supplemental Figure 2, A and B). Importantly, in both breast cancer cell lines MDA-MB-231 and SK-BR-3, MLN4924 significantly increased MFN1 and moderately increased MFN2, two proteins known to induce fusion (27), in dose- and time-dependent manners, while the levels of DRP1, a protein known to induce fission (28) remained unchanged (Figure 2, A and B, and Supplemental Figure 2, A and B). It is worth noting that NAEβ knockdown also increased MFN1 without affecting MFN2 and DRP1 (Figure 1F).

It has been previously shown that DRP1 shuttling between the cytosol and mitochondria could regulate mitochondrial dynamics (28). To further elucidate potential involvement of DRP1 in MLN4924's effects, we measured the cellular distribution of DRP1. Interestingly, as compared with the vehicle control, MLN4924 treatment significantly increased cytoplasmic DRP1, but remarkably decreased mitochondrial DRP1 (Figure 2, C and D, and Supplemental Figure 2, C and D). Since the retention of DRP1 in mitochondria is tightly regulated by its phosphorylation at serine residue 616 ($DRP1^{S616}$) (29), we then determined whether the reduction in mitochondrial DRP1 is associated with altered $DRP1^{S616}$ levels. Indeed, MLN4924 significantly reduced the phospho-$DRP1^{S616}$ level in the mitochondrial fractions (Figure 2, C and E, and Supplemental Figure 2, C and E), while it slightly increased it in the cytoplasmic fraction. Thus, by suppressing mitochondrial DRP1 phosphorylation on Ser^{616}, MLN4924 reduced DRP1 recruitment to mitochondria. Taken together, these results indicate that an increase in fusion-promoting proteins, particularly MFN1, and a decrease in mitochondrial fusion–suppressing protein DRP1, are associated with fission-to-fusion conversion induced by MLN4924.

MFN1, MFN2, and DRP1 are responsible for fusion conversion. We next determined whether alterations in the levels of MFN1/2 and DRP1 are causally related to the observed fission-to-fusion conversion. MFN1 or MFN2 was individually knocked down via 2 independent siRNAs (Figure 2, F and G, and Supplemental Figure 2, F and G). MFN1 knockdown completely rescued MLN4924-induced fission-to-fusion conversion, whereas MFN2 knockdown caused approximately 70% rescue (Figure 2H and Supplemental Figure 2H). Similarly, ectopic expression of DRP1 showed 50% rescue of MLN4924-induced mitochondrial fusion (Figure 2I and Supplemental Figure 2I), while showing no effect on increased MFN1 and MFN2 levels by MLN4924 (Figure 2J and Supplemental Figure 2J). Collectively, these data indicate that increased MFN1 as well as MFN2, and decreased mitochondrial DRP1 are all responsible for MLN4924-induced mitochondrial fusion, with MFN1 playing a dominant role.

MLN4924-induced fusion is not due to G2/M arrest, but enhances cell survival. It has been previously reported that mitochondrial fusion is associated with cell cycle arrest, whereas MLN4924 indeed induced G2/M arrest in both breast cancer cell lines (30, 31). Therefore, we determined whether observed mitochondrial fusion is a consequence of the G2/M arrest. MLN4924 induced a dose-dependent increase of G2/M arrest in si-NC– or HA-vector–transfected cells; neither MFN1/MFN2 knockdown nor DRP1 overexpression had any effect (Figure 2K and Supplemental Figure 2K), indicating their dissociation. Notably, either MFN1/MFN2 knockdown or DRP1 overexpression significantly decreased cell survival (Figure 2, L and M, and Supplemental Figure 2, L and M), suggesting that mitochondrial fusion is a cellular defensive mechanism in response to MLN4924 cytotoxicity. Collectively, these results suggest that MLN4924-induced mitochondrial fusion is not the consequence of G2/M arrest, but rather an adaptive response for cell survival.

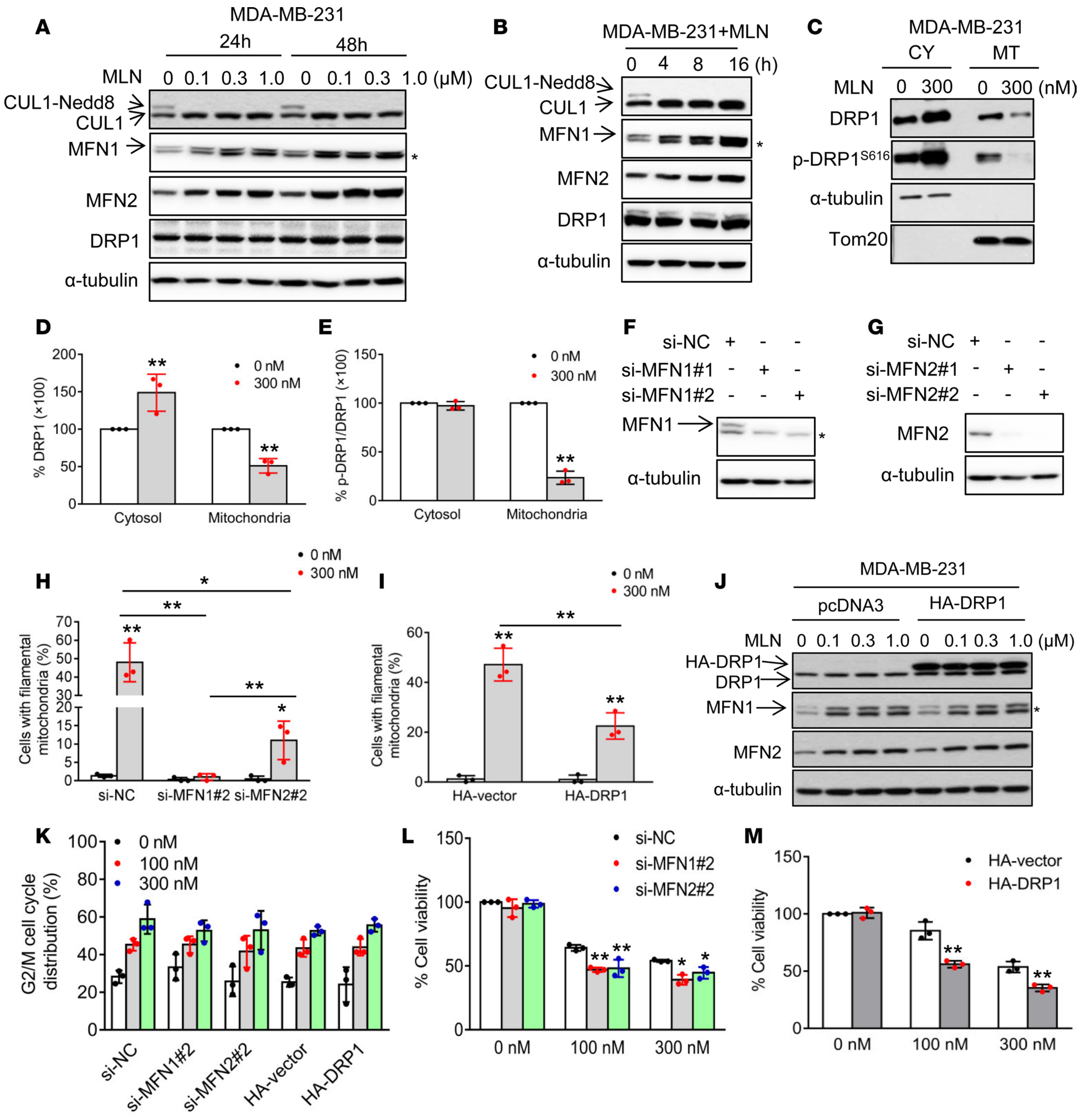

Figure 2. Mitochondrial dynamics regulators mediate MLN4924-induced mitochondrial fusion. (**A** and **B**) MDA-MB-231 cells were treated with various concentrations of MLN4924 for 24 or 48 hours (**A**), or treated with 300 nM MLN4924 for indicated time periods (**B**) and analyzed by Western blotting using the indicated antibodies. Asterisks in all Western blots indicate nonspecific bands. (**C**) MDA-MB-231 cells were treated with 300 nM MLN4924 for 24 hours and mitochondria were isolated. Cytoplasmic (CY) and mitochondrial (MT) fractions were analyzed by Western blotting. α-Tubulin and Tom20 served as markers for cytoplasmic and mitochondrial fractions, respectively. SE, short exposure; LE, long exposure. (**D**) DRP1 expression levels in cytosol and mitochondria in **C** were normalized to α-tubulin and Tom20, respectively. Results are shown as mean ± SD ($n = 3$). (**E**) Phosphorylated DRP1^{S616} levels in **C** were normalized to total DRP1 levels in indicated cellular fractions (mean ± SD, $n = 3$). (**F** and **G**) MDA-MB-231 cells were transfected with indicated siRNAs against MFN1 or MFN2. Forty-eight hours after transfection, cells were harvested and analyzed by Western blotting. (**H** and **I**) MDA-MB-231 cells were transfected with indicated siRNAs (**H**) or plasmids expressing HA-vector (**I**) for 24 hours, and then treated with 300 nM MLN4924 for another 24 hours. Cells were then stained with MitoTracker Red, and mitochondrial morphology was photographed by confocal microscopy. The interconnected filamentous mitochondria are quantified (mean ± SD, $n = 3$). (**J**) MDA-MB-231 cells were transfected with HA-vector or HA-DRP1 for 24 hours, followed by treatment with various concentrations of MLN4924 for another 24 hours before being analyzed by Western blotting. (**K**) MDA-MB-231 cells were transfected with indicated siRNAs against MFN1 or MFN2 and plasmids expressing HA-vector for 24 hours, treated with 100 or 300 nM MLN4924, followed by FACS analysis after 24 hours. Cells at the G2/M phase were plotted

(mean ± SD, $n = 3$). (**L**) MDA-MB-231 cells were transfected with si-NC, si-MFN1-2, or si-MFN2-2 for 24 hours, then treated with 100 or 300 nM MLN4924, followed by trypan blue exclusion assay for cell viability after 48 hours (mean ± SD, $n = 3$). (**M**) MDA-MB-231 cells were transfected with HA-vector and HA-DRP1 for 24 hours, then treated with 100 or 300 nM MLN4924, followed by trypan blue exclusion assay for cell viability after 48 hours (mean ± SD, $n = 3$). $^{*}P < 0.05$, $^{**}P < 0.01$ by 1-way ANOVA.

SCF$^{\beta\text{-TrCP}}$ E3 ligase mediates MFN1 ubiquitylation and degradation. To elucidate the mechanism(s) by which MLN4924 increased the levels of MFN1/2, we first focused on Parkin, a mitochondrial E3 known to be a neddylation substrate that promotes MFN1/2 ubiquitylation and degradation (32, 33). We used Parkin-null HeLa cells (34) and found that MLN4924 remained active to cause a dose-dependent increase of MFN1, with minor effects on MFN2 (Supplemental Figure 3A). Thus, involvement of Parkin was excluded for MLN4924-induced accumulation of MFN1/2.

We next turned our attention to CRL/SCF$^{\beta\text{-TrCP}}$ as a potential E3 ligase for targeted ubiquitylation and degradation of MFN1 after identifying an evolutionarily conserved β-TrCP degron motif (^{85}S<u>S</u>GKS<u>S</u>^{90}) on MFN1 (Supplemental Figure 3B). Given that MFN1 is a mitochondrial protein, we first determined whether the components of SCF are also localized in mitochondria. Indeed, cullin-1, β-TrCP1, and RBX1 were all detected in both cytosolic and mitochondrial fractions, with cullin-1 neddylation being inhibited by MLN4924 (Figure 3A and Supplemental Figure 3C). We then systematically examined whether MFN1 was a bona fide substrate of the SCF$^{\beta\text{-TrCP}}$ E3 ligase. First, we found that (a) exogenously expressed MFN1 and β-TrCP1 bound to each other by reciprocal immunoprecipitation experiments (Figure 3B and Supplemental Figure 3D), and (b) exogenously expressed MFN1 pulled down endogenous β-TrCP1 (Figure 3C). Together, these results showed that SCF$^{\beta\text{-TrCP}}$ E3 ligase interacts with MFN1 in mitochondria.

We then determined whether β-TrCP1 regulates MFN1 protein level and stability. Upon knockdown of both of β-TrCP1 and β-TrCP2, the MFN1 level was increased, along with the accumulation of Wee1, a known substrate of SCF$^{\beta\text{-TrCP}}$ E3 ligase (17), included as a positive control (Figure 3D). On the other hand, ectopic expression of β-TrCP1, but not its ligase-dead mutant β-TrCP1ΔF, reduced the levels of exogenously expressed MFN1 in a dose-dependent manner (Figure 3E and Supplemental Figure 3E), as well as endogenous MFN1 (Figure 3F and Supplemental Figure 3F). Furthermore, siRNA-based β-TrCP knockdown substantially extended the protein half-life of MFN1 (Figure 3, G and H, and Supplemental Figure 3, G and H). To determine whether the β-TrCP degron motif on MFN1 is important for β-TrCP binding and degradation, we mutated all serine residues to alanine (SSGKSS to AAGKSA, designated as MFN1 S85/85/90A), and found that the mutant MFN1 had a marked reduction in β-TrCP1 binding (Figure 3I), and much extended protein half-life. (Supplemental Figure 3I). Moreover, ectopically expressed β-TrCP1 substantially shortened the protein half-life of exogenously expressed wild-type MFN1, but not the mutant MFN1 in MDA-MB-231 (Figure 3, J and K) and SK-BR-3 (Supplemental Figure 3, J and K) cells. Furthermore, manipulation of β-TrCP by siRNA knockdown or ectopic expression caused an increase or decrease in the levels of endogenous MFN1, respectively, in multiple human lung cancer or bronchial epithelial cell lines (Supplemental Figure 3, L and M), suggesting that negative regulation of MFN1 stability by β-TrCP is a general phenomenon.

We further determined whether β-TrCP indeed promoted MFN1 ubiquitylation. The in vivo ubiquitylation assay showed that wild-type β-TrCP1, but not the β-TrCP1ΔF mutant, promoted polyubiquitylation of MFN1. However, wild-type β-TrCP1 failed to promote polyubiquitylation of the MFN1 S85/86/90A mutant with the degron motif abrogated (Figure 3L). Thus, the MFN1 degron motif determines the β-TrCP binding and subsequent ubiquitylation and degradation of MFN1. Finally, we determined the biological consequence of MFN1 degradation by SCF$^{\beta\text{-TrCP}}$ E3 ligase, and found that, like MLN4924 treatment, β-TrCP knockdown significantly increased filamentous mitochondria (Figure 3M). Taken together, our results support the notion that MLN4924-induced fission-to-fusion conversion is mediated by inactivation of SCF$^{\beta\text{-TrCP}}$ E3 ligase and subsequent accumulation of MFN1.

Global metabolic profiling identifies alterations in energy metabolism. We next used mass-spectrometry-based metabolic profiling to investigate the overall effect of neddylation inhibition on cell metabolism at a global level. MDA-MB-231 cells were treated with MLN4924 in 3 independent experiments, and an untargeted metabolomics strategy was applied to analyze cell extracts and culture supernatants. In a partial least squares discriminant analysis (PLS-DA) model, both the cell extracts (Figure 4A) and culture supernatants (Figure 4B) exhibited close clustering among triplicates of MLN4924-treated samples, far apart from DMSO control samples, suggesting prominent alterations of metabolites after neddylation blockage.

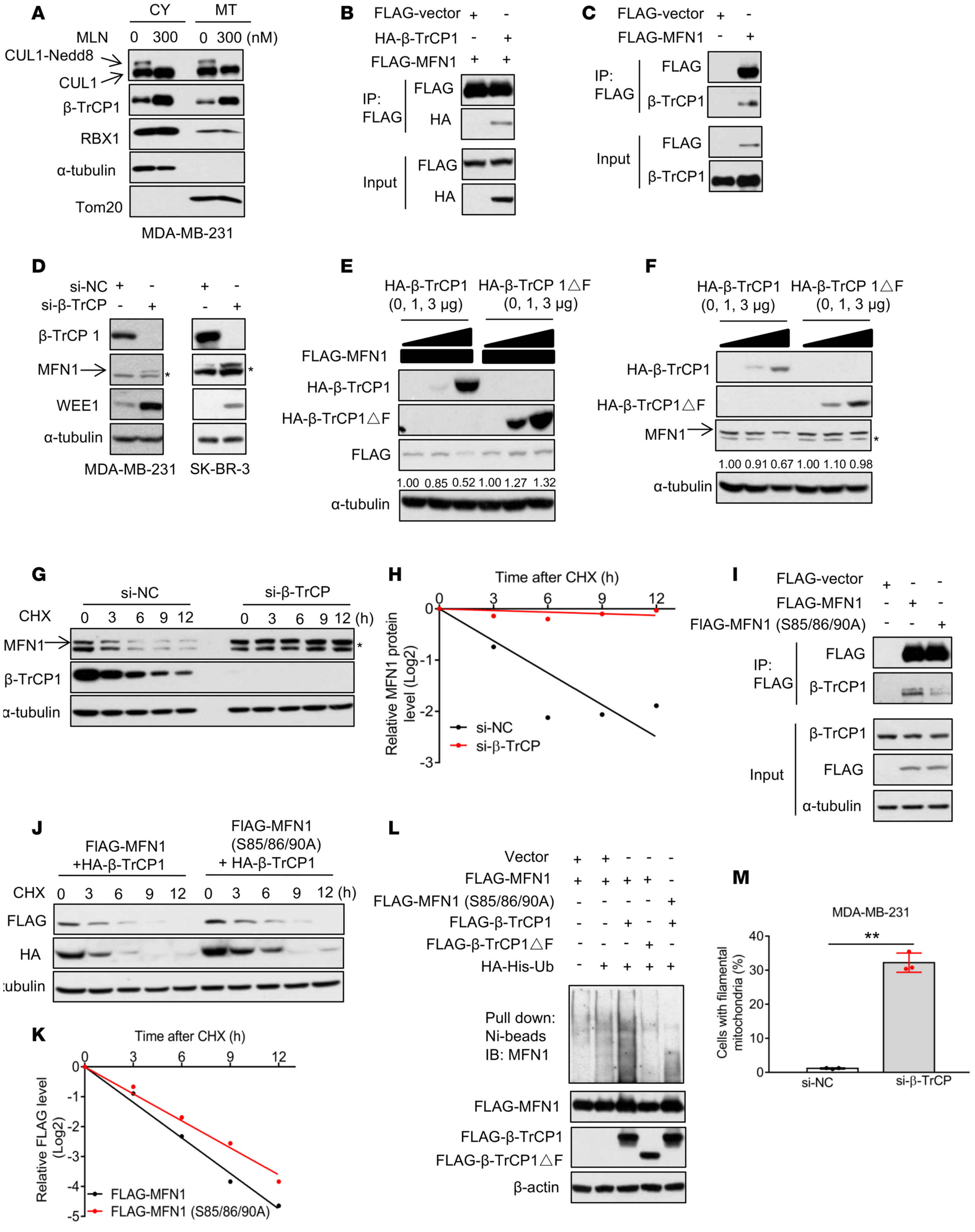
A
CY
MT
MLN
0
300
0
300 (nM)
CUL1-Nedd8
CUL1
β-TrCP1
RBX1
α-tubulin
Tom20
MDA-MB-231
B
FLAG-vector + -
HA-β-TrCP1 - +
FLAG-MFN1 + +
IP: FLAG
FLAG
HA
Input
FLAG
HA
C
FLAG-vector + -
FLAG-MFN1 - +
IP: FLAG
FLAG
β-TrCP1
Input
FLAG
β-TrCP1
D
si-NC + - + -
si-β-TrCP - + - +
β-TrCP 1
MFN1
*
WEE1
α-tubulin
MDA-MB-231
SK-BR-3
E
HA-β-TrCP1 (0, 1, 3 μg)
HA-β-TrCP 1△F (0, 1, 3 μg)
FLAG-MFN1
HA-β-TrCP1
HA-β-TrCP1△F
FLAG
1.00 0.85 0.52 1.00 1.27 1.32
α-tubulin
F
HA-β-TrCP1 (0, 1, 3 μg)
HA-β-TrCP 1△F (0, 1, 3 μg)
HA-β-TrCP1
HA-β-TrCP1△F
MFN1
*
1.00 0.91 0.67 1.00 1.10 0.98
α-tubulin
G
si-NC
si-β-TrCP
CHX
0 3 6 9 12 0 3 6 9 12 (h)
MFN1
*
β-TrCP1
α-tubulin
H
Time after CHX (h)
0 3 6 9 12
Relative MFN1 protein level (Log2)
0
-1
-2
-3
si-NC
si-β-TrCP
I
FLAG-vector + - -
FLAG-MFN1 - + -
FlAG-MFN1 (S85/86/90A) - - +
IP: FLAG
FLAG
β-TrCP1
Input
β-TrCP1
FLAG
α-tubulin
J
FlAG-MFN1 +HA-β-TrCP1
FlAG-MFN1 (S85/86/90A) + HA-β-TrCP1
CHX
0 3 6 9 12 0 3 6 9 12 (h)
FLAG
HA
tubulin
K
Time after CHX (h)
0 3 6 9 12
Relative FLAG level (Log2)
0
-1
-2
-3
-4
-5
FLAG-MFN1
FLAG-MFN1 (S85/86/90A)
L
Vector + + - - -
FLAG-MFN1 + + + + -
FLAG-MFN1 (S85/86/90A) - - - - +
FLAG-β-TrCP1 - - + - +
FLAG-β-TrCP1△F - - - + -
HA-His-Ub - + + + +
Pull down: Ni-beads IB: MFN1
FLAG-MFN1
FLAG-β-TrCP1
FLAG-β-TrCP1△F
β-actin
M
MDA-MB-231
**
Cells with filamental mitochondria (%)
40
30
20
10
0
si-NC
si-β-TrCP

Figure 3. SCF$^{\beta\text{-TrCP}}$ E3 ligase controls MFN1 turnover and regulates mitochondrial dynamics. (**A**) MDA-MB-231 cells were treated with 300 nM MLN4924 for 24 hours and mitochondria were isolated. Cytoplasmic (CY) and mitochondrial (MT) fractions were analyzed by Western blotting with indicated antibodies. α-Tubulin and Tom20 served as markers for cytoplasmic and mitochondrial fractions, respectively. (**B** and **C**) HEK293 cells were transfected with indicated plasmids, immunoprecipitated with FLAG-agarose beads, and analyzed by Western blotting to detect exogenous (**B**) or endogenous (**C**) β-TrCP1. (**D**) MDA-MB-231 and SK-BR-3 cells were transfected with si-NC or siRNA targeting β-TrCP1/2 for 48 hours and cells were then analyzed by Western blotting. Asterisks in Western blots indicate nonspecific bands. (**E** and **F**) MDA-MB-231 cells were cotransfected with MFN1 and increasing amounts of β-TrCP1 or β-TrCP1ΔF (**E**), or transfected with increasing amounts of β-TrCP1 or β-TrCP1ΔF alone (**F**) for 48 hours. Cells were then analyzed by Western blotting. The band density was quantified by ImageJ and normalized to α-tubulin. (**G** and **H**) MDA-MB-231 cells were transfected with si-NC or siRNA targeting β-TrCP1/2 for 48 hours, then incubated with CHX for indicated periods of time. (**G**) Cells were collected and analyzed by Western blotting. (**H**) MFN1 band density in **G** was quantified using ImageJ software and normalized to α-tubulin, then normalized to $t = 0$ time point. (**I**) HEK293 cells were transfected with indicated plasmids, immunoprecipitated with FLAG-agarose beads and analyzed by Western blotting to detect endogenous β-TrCP1. (**J** and **K**) MDA-MB-231 cells were cotransfected with β-TrCP1 and MFN1 or MFN1 S85/85/90A mutant for 48 hours, then incubated with CHX for indicated periods of time. (**J**) Cells were collected and analyzed by Western blotting. (**K**) The band density of FLAG-MFN1 in **J** was quantified using ImageJ software and normalized to α-tubulin, then normalized to $t = 0$ time point. (**L**) HEK293 ells were transfected with indicated plasmids and lysed under denaturing conditions, followed by Ni-bead pulldown. Washed beads were boiled and analyzed by Western blotting for MFN1. (**M**) MDA-MB-231 cells were transfected with either si-NC or siRNA targeting β-TrCP1/2 for 48 hours. Cells were stained with MitoTracker Red, and mitochondrial morphology was photographed by confocal microscopy. The percentage of cells with interconnected filamentous mitochondria was quantified. Results are shown as mean ± SD ($n = 3$). $^{**}P < 0.01$ by 1-way ANOVA.

We next defined the overall metabolic alterations induced by neddylation inhibition, using the values of variable importance in the projection (VIP) as the indicator to generate heatmaps (Figure 4, C and D) and V-plots (Supplemental Figure 4, A and B). Indeed, MLN4924 treatment caused significant inhibition of overall metabolism in cell extracts (Figure 4C, shown in green), with less effect on culture supernatants (Figure 4D). The changed metabolites include carbohydrates, organic acids, amino acids, nucleotides, and lipids (Figure 4, C and D). Among the most remarkably altered metabolites, 3-phosphoglyceric acid and pyruvic acid were significantly increased, whereas succinic acid and fumaric acid were substantially decreased (Supplemental Figure 4C). Importantly, these perturbed metabolites are the components of glycolysis and the mitochondrial tricarboxylic acid (TCA) cycle (Supplemental Figure 4D), respectively, indicating an enhanced glycolysis and reduced mitochondrial function upon neddylation inhibition. Thus, neddylation blockage altered global metabolic profiling and energy metabolism by modulating glycolysis and OXPHOS.

MLN4924 inhibits multiple mitochondrial functions. Having established that neddylation blockage affects both mitochondrial morphology and TCA cycle, whereas mitochondrial dynamics are closely associated with mitochondrial functions and cellular metabolic operations (9), we next determined potential effects of MLN4924 precisely on mitochondrial integrity and functions. First, we measured the mitochondrial oxygen consumption rate (OCR) using a Seahorse XF96 Analyzer (Figure 5, A and B, and Supplemental Figure 5, A and B), and found that MLN4924 remarkably stimulated basal OCR (Figure 5C and Supplemental Figure 5C), ATP-linked OCR (Figure 5D and Supplemental Figure 5D), proton-leak OCR (Figures 5E and Supplemental Figure 5E), maximal OCR (Figure 5F and Supplemental Figure 5F), and non-mitochondrial OCR (Figure 5G and Supplemental Figure 5G), while it significantly suppressed reserve-capacity OCR (Figure 5H and Supplemental Figure 5H).

To determine the potential role of MFN1 in MLN4924-induced alterations in OCR or extracellular acidification rate (ECAR), we performed a rescue experiment by the siRNA knockdown approach. MFN1 knockdown (by siMFN1) significantly reduced MLN4924-induced basal OCR (Supplemental Figure 6, A and B, and Supplemental Figure 7, A and B) and ATP-linked OCR (Supplemental Figures 6C and 7C) in both breast cancer cell lines. However, the rescue effects on proton-leak OCR (Supplemental Figures 6D and 7D), maximal OCR (Supplemental Figures 6E and 7E), non-mitochondrial OCR (Supplemental Figures 6F and 7F), and reserve-capacity OCR (Supplemental Figures 6G and 7G) were partially seen in MDA-MB231 cells, but not in SK-BR3 cells. Taken together, these results suggest that MLN4924-induced MFN1 accumulation is partially responsible for observed alterations in OCR, the extent of which is cell-line dependent.

We also measured the intracellular ATP levels and found that MLN4924 significantly decreased ATP production (Figure 5I and Supplemental Figure 5I). We then determined possible changes in mitochondrial membrane potential, a critical indicator of mitochondrial integrity and homeostasis (35), and found that MLN4924 caused a significant reduction of mitochondrial depolarization (Figure 5J and Supplemental Figure 5J). We further found that MLN4924 caused a significant increase in mitochondrial DNA (mtDNA) copy number (Figure 5K and Supplemental Figure 5K). Finally, we measured mitochondrial ROS (mito-ROS) levels, and found that MLN4924 caused an increase of mito-ROS (Figure 5L and Supplemental Figure 5L). All these effects were found to be in dose- and time-dependent manners. Collectively, these results

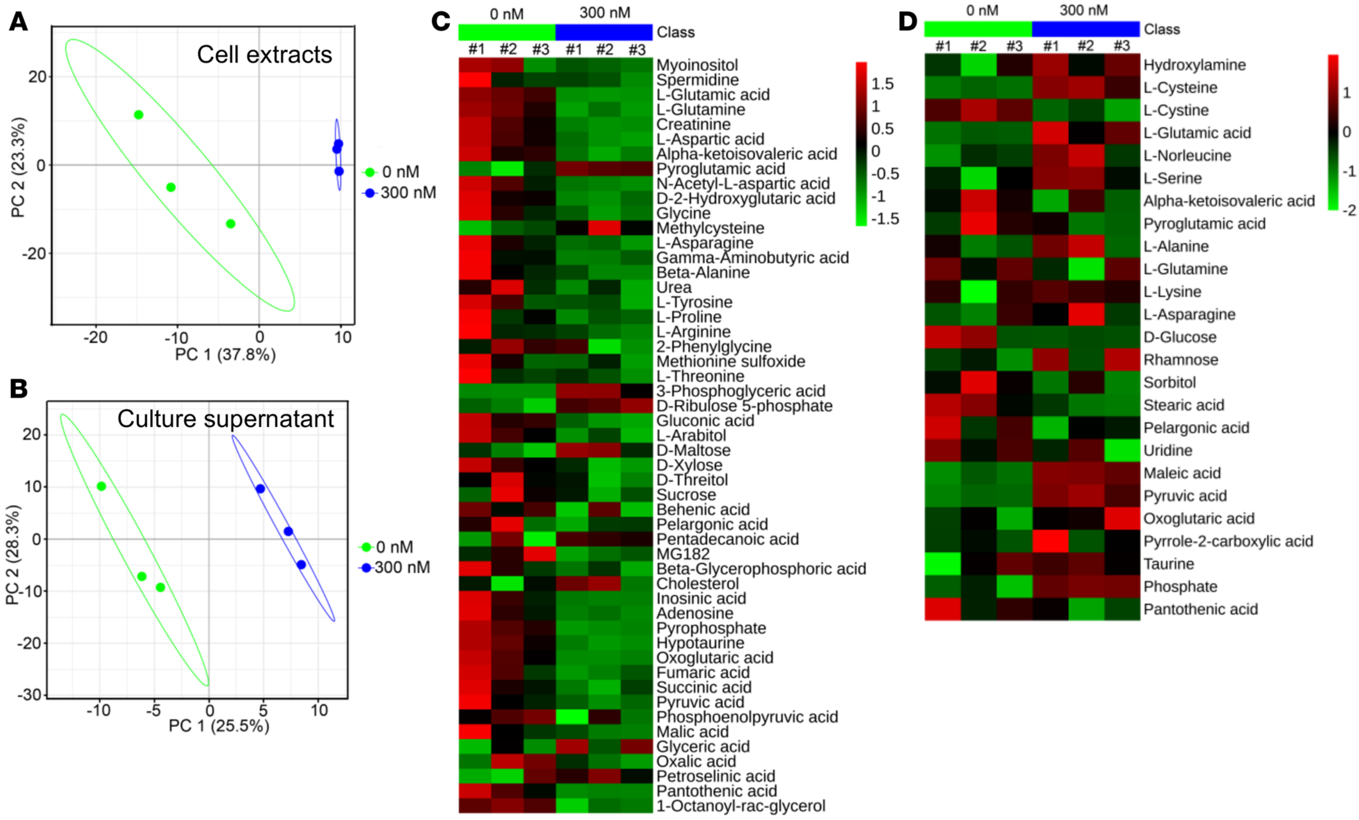

Figure 4. Mass-spectrometry-based metabolic profiling. (**A** and **B**) MDA-MB-231 cells were treated with DMSO or 300 nM MLN4924 for 24 hours, and cell extracts (**A**) and culture supernatants (**B**) were subjected to untargeted metabolic profiling analysis. Shown is the PLS-DA score plot from 3 independent preparations of cell extracts/supernatants. (**C** and **D**) Metabolites in **A** and **B** with VIP (variable importance in the projection) value greater than 1 are displayed in a heatmap format. Colors represent the levels of the metabolites from low (green) to high (red).

demonstrated that MLN4924 effectively impairs mitochondrial integrity and functions, while increasing the mitochondrial respiration, but with reduced ATP production.

MLN4924 promotes glycolysis via increased PKM2 activation. Cancer cells often increase their glycolytic activity to ensure energy supply when mitochondrial function is impaired (5). To further explore potential impacts of MLN4924 on glycolysis, we measured ECAR, an indicator of glycolysis, and found that MLN4924 treatment caused a substantial increase in media acidification in time- and dose-dependent manners (Figure 6, A and B, and Supplemental Figure 8, A and B). This effect appeared to be independent of MFN1 accumulation, since MFN1 knockdown had little, if any, rescue effect, although it in general reduced the ECAR value in MDA-MB231 cells (Supplemental Figures 6H and 7H), suggesting that MFN1 is not involved in MLN4924-induced enhancement of glycolysis.

Consistent with increased ECAR, MLN4924 increased cellular utilization of glucose (Figure 6C and Supplemental Figure 8C), production of glycolytic end products, such as pyruvate (Figure 6D and Supplemental Figure 8D) and lactate (Figure 6E and Supplemental Figure 8E), and significantly increased PK activity in time- and dose-dependent manners (Figure 6F and Supplemental Figure 8F). We next investigated whether MLN4924-induced PK activity is PKM2 dependent, and found that PKM2 knockdown (Figure 6G and Supplemental Figure 8G) completely abrogated MLN4924 induction of PK activity at all doses tested (Figure 6H and Supplemental Figure 8H), indicating it is a purely PKM2-dependent event. Given that PKM2 could exist as a monomer, homodimer, or homotetramer, with the homotetrameric form being the most enzymatically active (12), we determined whether MLN4924 would trigger the formation of PKM2 tetramers using glutaraldehyde crosslinking coupled with a Western blot assay. Indeed, MLN4924 increased the levels of PKM2 tetramers in a dose-dependent manner (Figure 6I and Supplemental Figure 8I). Furthermore, using bacterially expressed and purified PKM2 protein (Figure 6J, elution fractions 1 and 2 were used) in an in vitro biochemical assay, we found that MLN4924 increased PKM2 activity (Figure 6K), with slightly greater efficacy than SAICAR (Supplemental Figure 8J), a known PKM2 activator (36). Finally, we

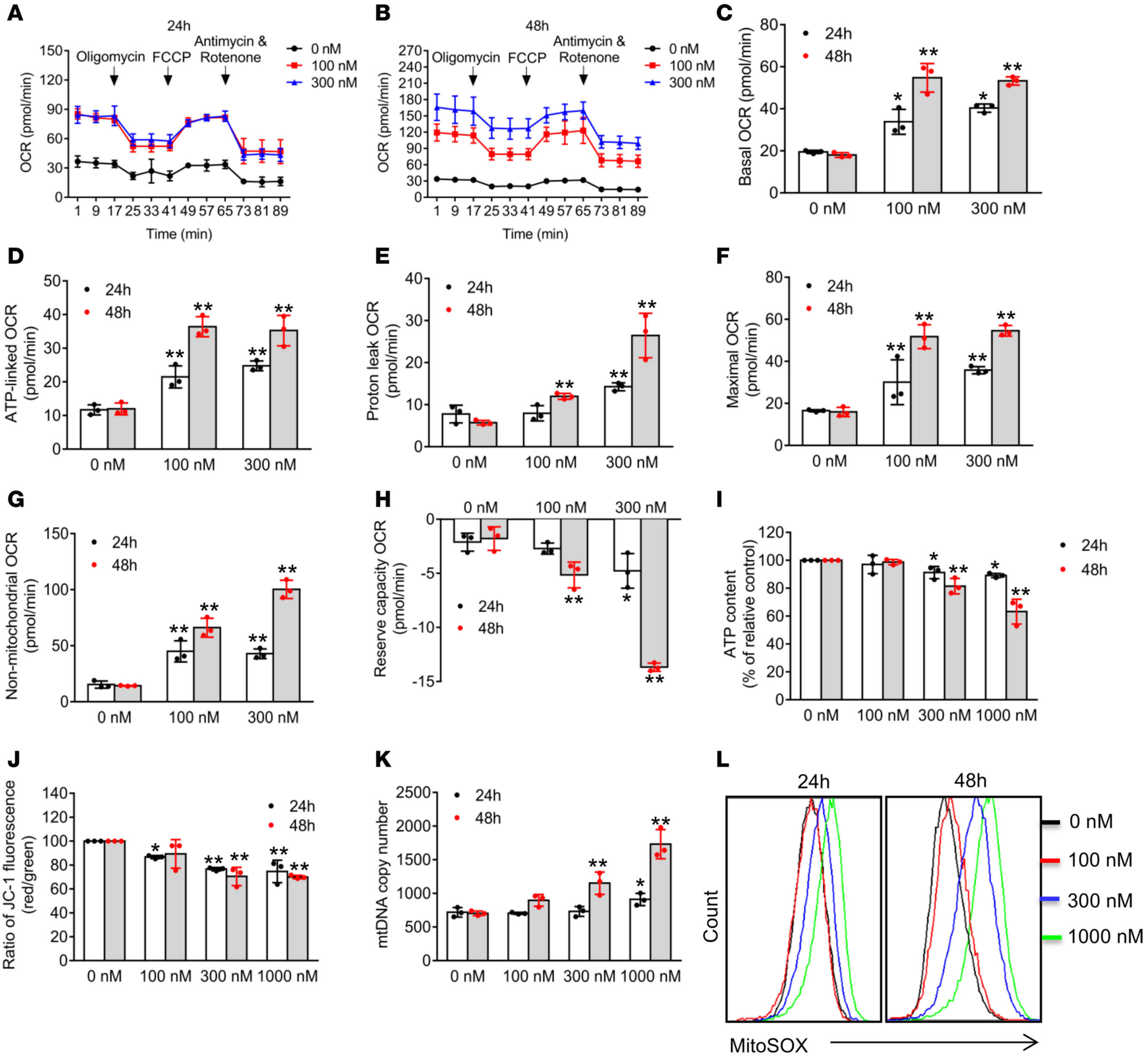

Figure 5. MLN4924 inhibits mitochondrial functions. (**A**–**H**) MDA-MB-231 cells were treated with indicated concentrations of MLN4924 for 24 and 48 hours, then subjected to determination of real-time OCR (**A** and **B**). Basal OCR (**C**), ATP-linked OCR (**D**), proton-leak OCR (**E**), maximal OCR (**F**), non-mitochondrial OCR (**G**), and reserve-capacity OCR (**H**) were calculated from data shown in **A** and **B** (mean ± SD, $n = 3$). (**I**–**K**) MDA-MB-231 cells were treated with indicated concentrations of MLN4924 for 24 and 48 hours, then subjected to analysis for ATP production (**I**), mitochondrial membrane potential (**J**), and mtDNA copy number (**K**) (mean ± SD, $n = 3$). (**L**) MDA-MB-231 cells were treated with indicated concentrations of MLN4924 for 24 and 48 hours, and mitochondrial ROS generation was determined using the mitochondrial superoxide indicator MitoSOX Red. Fluorescence was measured using a FACS instrument. Similar results were obtained from 3 independent experiments. $*P < 0.05$, $**P < 0.01$ by 1-way ANOVA.

determined the biological significance of MLN4924 activation of PKM2, a critical mediator of enhanced glycolysis, and found that PKM2 knockdown significantly decreased cell growth and clonogenic survival induced by MLN4924 (Figure 6, L and M, and Supplemental Figure 8, K and L). Taken together, our data demonstrated that via inducing homotetramer formation, MLN4924 activates PKM2 to promote glycolysis, which plays a protective role in response to MLN4924 cytotoxicity.

Enhanced cancer cell killing by cotargeting neddylation and OXPHOS or glycolysis. Fused mitochondria are usually considered energetically active through OXPHOS, which is commonly associated with cytoprotective functions (9). Given that MLN4924-induced mitochondrial fusion is accompanied with increased OXPHOS, we

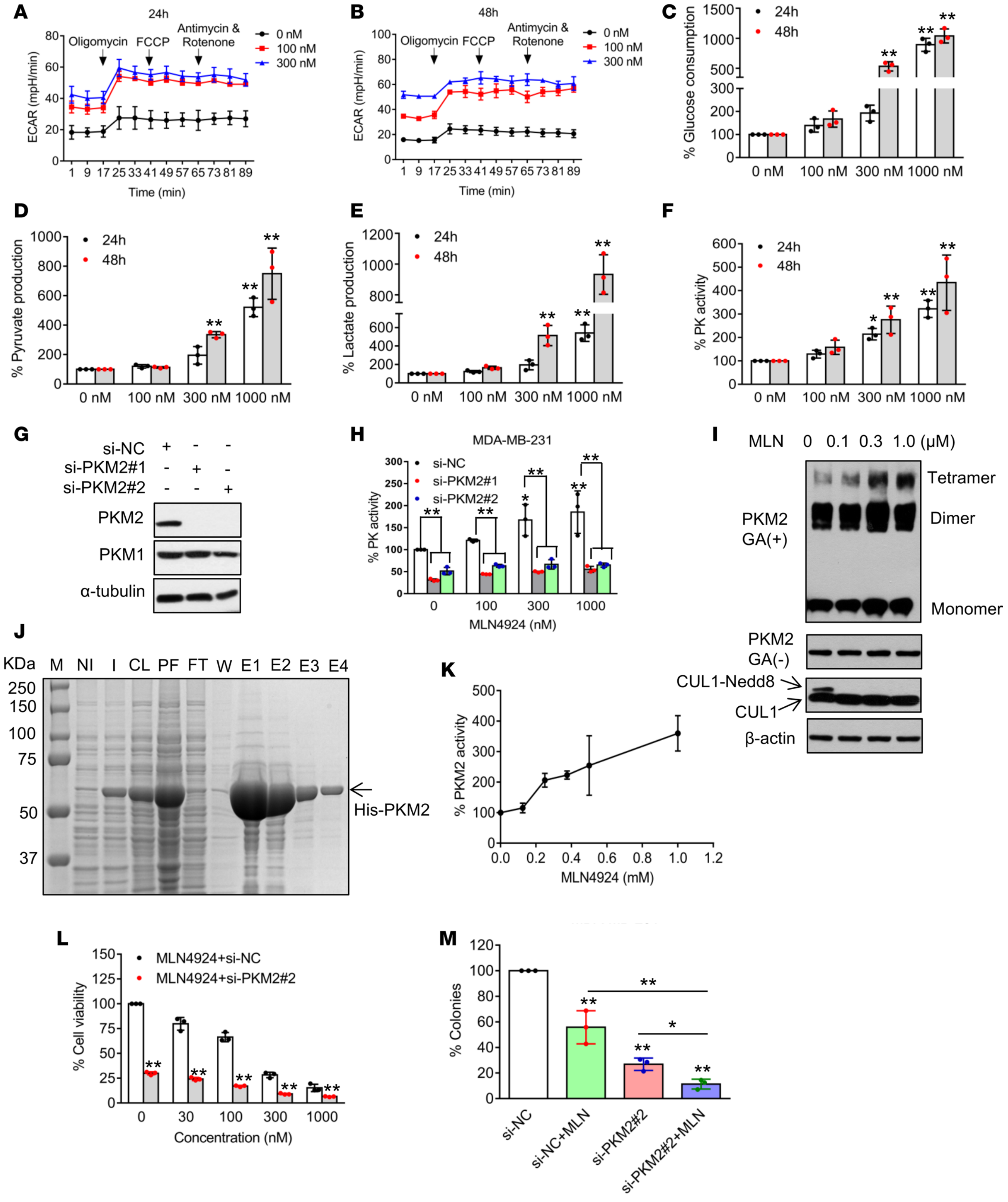

Figure 6. MLN4924 promotes glycolysis. (**A** and **B**) MDA-MB-231 cells were treated with indicated concentrations of MLN4924 for 24 and 48 hours, and then subjected to analysis for ECAR, which was recorded simultaneously while obtaining OCR data in Figure 5, A and B. (**C**–**F**) MDA-MB-231 cells were treated with indicated concentrations of MLN4924 for 24 and 48 hours, and then the culture media were collected to analyze glucose consumption (**C**), pyruvate (**D**), and lactate (**E**) production, whereas cells were collected to measure pyruvate kinase activity (**F**) (mean ± SD, *n* = 3). (**G**) MDA-MB-231 cells were transfected with scrambled control siRNA (si-NC), or 2 independent siRNAs targeting PKM2 (si-PKM2-1, si-PKM2-2). Forty-eight hours after transfection, cells were harvested for Western blotting. (**H**) MDA-MB-231 cells were transfected with indicated siRNAs for 24 hours, then treated with various concentrations of MLN4924 for another 24 hours, and then collected to measure pyruvate kinase activity (mean ± SD, *n* = 3). (**I**) MDA-MB-231 cells were

treated with indicated concentrations of MLN4924 for 24 hours, crosslinked using glutaraldehyde, and analyzed by Western blotting. GA, glutaraldehyde. (**J**) Purification of PKM2. Bacterially expressed PKM2 was induced by IPTG, followed by sonication, Ni-column purification and elution. An aliquot of each fraction was subjected to PAGE, followed by Coomassie blue staining. M, molecular marker; NI, noninduced cells; I, induced cells; CL, cleared cell lysate; PF, precipitate fraction; FT, flow through; W, wash fraction; E, elution. (**K**) Pyruvate kinase activity of purified human PKM2 (from elution fractions 1 and 2) in the presence of increasing concentrations of MLN4924. (**L**) MDA-MB-231 cells were transfected with either si-NC or si-MFN2-2 for 24 hours, and then treated with various concentrations of MLN4924 for 72 hours and cell viability was detected by trypan blue exclusion assay (mean ± SD, $n = 3$). (**M**) MDA-MB-231 cells were transfected with either si-NC or si-MFN2-2, and then treated with DMSO control or 5 nM MLN4924 for 10 days. Colonies were stained and counted. Data shown as mean ± SD ($n = 3$). $^*P < 0.05$, $^{**}P < 0.01$ by 1-way ANOVA.

determined whether metformin, an inhibitor of mitochondrial complex I that blocks OXPHOS (37), would sensitize breast cancer cells to MLN4924. We first determined the growth inhibitory effect of metformin as a single agent on 2 breast cancer cell lines (Supplemental Figure 9, A and B), and used its IC_{25} dose in combination with various doses of MLN4924. Indeed, metformin significantly sensitized cancer cells to MLN4924 at all doses tested (Figure 7A and Supplemental Figure 9C). Similarly, the combination also caused significantly more inhibition of clonogenic survival than the single agent (Figure 7C and Supplemental Figure 9D). Thus, by OXPHOS inhibition, metformin at low IC_{25} dose significantly sensitized breast cancer cells to MLN4924.

Given that PKM2 activation confers cellular survival, we next investigated whether shikonin, a specific PKM2 inhibitor (13), would also sensitize breast cancer cells to MLN4924. We first determined the growth inhibitory effect of shikonin as a single agent on 2 breast cancer cell lines (Supplemental Figure 9, E and F), and used its IC_{25} dose in combination with various doses of MLN4924. Again, shikonin significantly enhanced MLN4924-induced suppression of cell growth at all doses used (Figure 7B and Supplemental Figure 9G). The combination also significantly reduced the clonogenic survival of cancer cells (Figure 7C and Supplemental Figure 9D). Thus, by inhibition of PKM2 and subsequent glycolysis, shikonin, at low IC_{25} dose, sensitized breast cancer cells to MLN4924.

Finally, we used in vivo xenograft tumor models of both MDA-MB-231 and SK-BR-3 cells to assess the anticancer efficacy of MLN4924, metformin, or shikonin acting alone or in combinations at nontoxic doses (Supplemental Figure 9, H and I). In both models, compared with vehicle control, tumor growth was moderately (but significantly) inhibited by the treatment with a single agent, and further inhibited (also significantly) by combination of MLN4924 with either metformin or shikonin (Figure 7, D and G). Analysis of tumor weight harvested at the end of the experiments also showed a statistically significant difference between vehicle-treated tumors and those treated with a combination (Figure 7, E and H). We further estimated the time period for tumors to double in size, and found that vehicle-treated mice had the shortest doubling time, followed by single-agent treatment. The combined treatment showed the longest time period for tumor doubling (Figure 7, F and I). Together, these data indicated that blockage of neddylation triggers OXPHOS and glycolysis, and a neddylation inhibitor should, therefore, be used in combination with inhibitors of OXPHOS or glycolysis to significantly enhance its anticancer efficacy. Our study provides a sound strategy for mechanism-based combined target therapy.

Discussion

Abnormal energy metabolism is one of the well-characterized tumor hallmarks, and therapeutic targeting of such abnormality has drawn increasing attention (3, 38). Here, we report the unexpected finding that neddylation blockage by its inhibitor MLN4924 induced mitochondrial fission-to-fusion conversion, altered mitochondrial function, and promoted glycolysis, and that the therapeutic combination of MLN4924 with the OXPHOS inhibitor metformin or the glycolysis inhibitor shikonin significantly increased anticancer efficacy in both in vitro and in vivo models.

Mitochondrial fusion and fission dynamics is a complicated process that is regulated by a variety of factors (8). Here, we made the observation that neddylation indeed regulates this process. That is, blockage of neddylation induced the fission-to-fusion conversion (Figure 1), with the mechanism involving 3 key regulators of mitochondrial morphology, MFN1, MFN2, and DRP1. Specifically, we found that MLN4924 increased the levels of the 2 fusion-promoting factors MFN1 and MFN2 by blocking their degradation, but decreased mitochondrial recruitment of the fusion-inhibiting factor DRP1 by reducing its phosphorylation on Ser^{616}. Notably, these alterations played a causal role, since knockdown of MFN1/2 or ectopic expression of DRP1 completely or partially reversed the status from fusion back to fission (Figure 2). It is worth noting that MFN1 knockdown completely, whereas MFN2 knockdown partially, inhibited MLN4924-induced mitochondrial fusion, indicating a key role of MFN1 in the process, consistent with a previous report in other

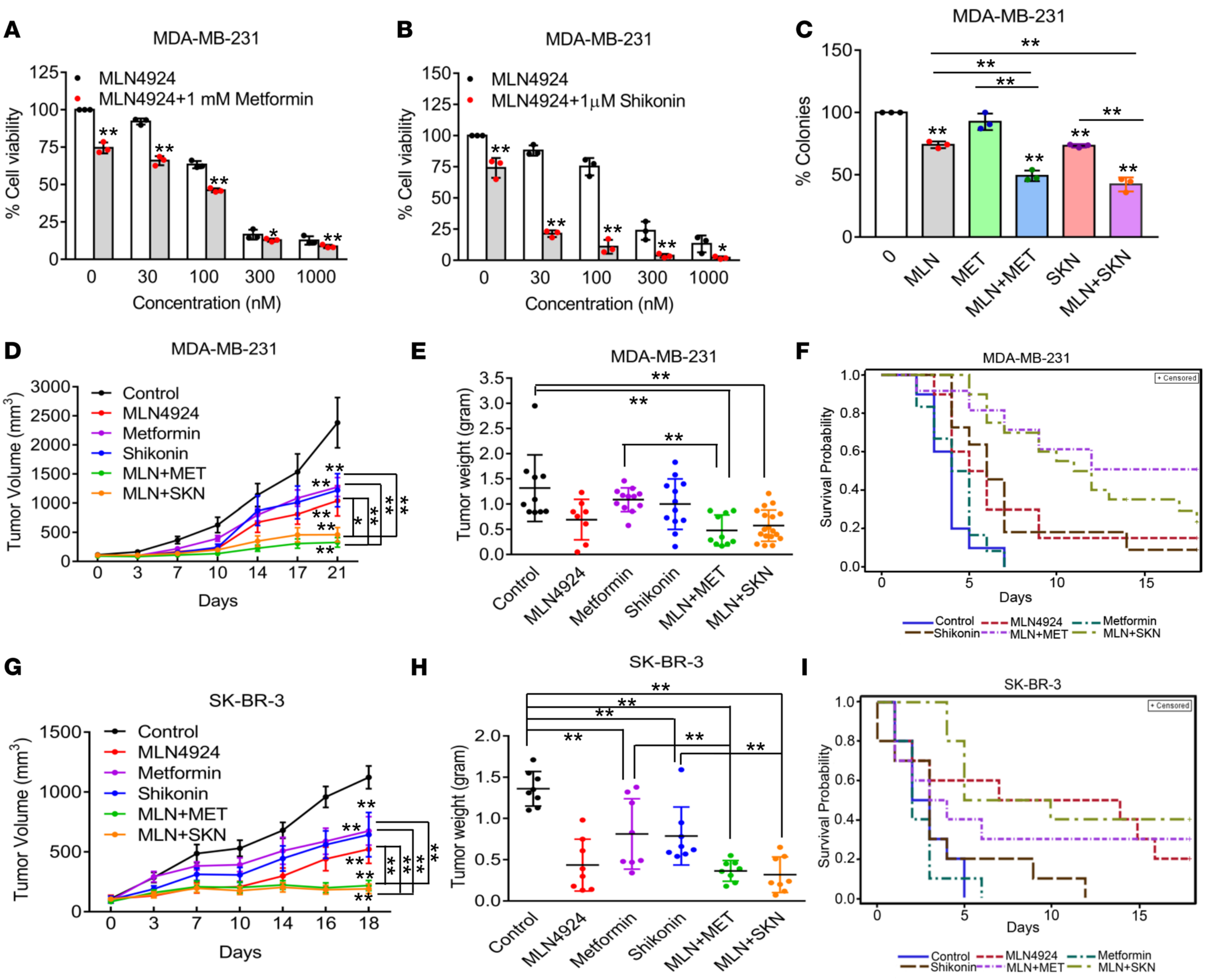

Figure 7. Combined targeting of neddylation and OXPHOS or PKM2. (**A** and **B**) MDA-MB-231 cells were treated with various concentrations of MLN4924 in the absence or presence of 1 mM metformin (**A**) or 1 μM shikonin (**B**) for 72 hours and cell number was counted by trypan blue exclusion assay (mean ± SD, *n* = 3). **P* < 0.05, ***P* < 0.01 by 1-way ANOVA. (**C**) MDA-MB-231 cells were treated with 5 nM MLN4924, 0.25 mM metformin (MET), or 0.15 μM shikonin (SKN), alone or in combination to measure clonogenic survival (mean ± SD, *n* = 3). ***P* < 0.01 by 1-way ANOVA. (**D** and **E**) In vivo growth of MDA-MB-231 xenograft tumors (**D**) after 21 days of treatment with MLN4924, metformin, or shikonin, alone or in combination, and tumor weight (**E**) at the end of the experiment (*n* = 8–18). **P* < 0.05, ***P* < 0.01 by 1-way ANOVA for tumor weight and 2-way ANOVA for tumor volume. (**F**) Time periods for MDA-MB-231 xenograft tumors to double in volume in SCID mice after each indicated treatment. (**G** and **H**) In vivo growth of SK-BR-3 xenograft tumors (**G**) after 18 days of treatment with MLN4924, metformin, or shikonin, alone or in combination, and tumor weight (**H**) at the end of the experiment (*n* = 8). **P* < 0.05, ***P* < 0.01 by 1-way ANOVA for tumor weight and 2-way ANOVA for tumor volume. (**I**) Time periods for SK-BR3 xenograft tumors to double in volume in nude mice after each indicated treatment. Death is defined here as tumor volume doubling.

model systems (27). Moreover, despite the observation that ectopic DRP1 expression inhibits MLN4924-induced mitochondrial fusion, the effect is partial, likely due to the fact that DRP1-mediated mitochondrial fission requires coordinated receptors on the mitochondrial outer membrane, proper posttranslational modifications, and different cellular structures such as the ER and actin (39). Nevertheless, our study did show that reduced mitochondrial transport of DRP1 is associated with reduced DRP1 phosphorylation on Ser^{616}. Importantly, we showed that approaches to block mitochondrial fusion, such as knockdown of MFN1 or MFN2 or ectopic expression of DRP1 further enhanced MLN4924-induced growth suppression, suggesting that mitochondrial fusion is a cellular protective mechanism against MLN4924 cytotoxicity (Figure 2), consistent with the notion that increased fusion facilitates cell survival (40). Our study, therefore, further expands the cellular survival signals triggered by MLN4924 from autophagy (20) to mitochondrial fusion.

Studies in yeast and mammalian cells have revealed that ubiquitin-proteasome-dependent degradation controls the levels of MFN1/2. In yeast, mitochondrial SCF$^{\mathrm{Mdm30}}$ E3 ligase mediates mitofusin Fzo1 ubiquitylation and degradation (41). In mammalian cells, E3 ligases such as MARCH5 and Parkin have been shown to promote degradation of MFN1/2 (32, 33, 42). In our study, we found that the MLN4924-induced MFN1/2 increase is independent of Parkin (Supplemental Figure 3A), but dependent on SCF$^{\beta\mathrm{TrCP}}$, also known as CRL1, the founding member of the CRL family, which is inactivated by MLN4924 via cullin deneddylation, leading to accumulation of substrates such as MFN1 (16, 25). Although two F-box proteins, Fbxl4 and Fbxl7, were reported to regulate mitochondrial dynamics in mammalian cells (43, 44), to our knowledge no F-box protein has been previously reported to target MFN for ubiquitylation and degradation. We showed here that F-box protein β-TrCP binds to MFN1 in a degron-motif-dependent manner to promote its ubiquitylation and degradation. Thus, by inactivating cullin-1 via blocking its neddylation, MLN4924 caused MFN1 accumulation. Importantly, like MLN4924 treatment, β-TrCP knockdown triggered mitochondrial fission-to-fusion conversion, demonstrating its functional significance. MFN1, therefore, joins a growing list of β-TrCP substrates (17).

Given that MLN4924 significantly induced mitochondrial fusion, it likely would impair mitochondrial functions. Furthermore, although neddylation modification has affected many aspects of cancer biology (15), no previous studies to our knowledge have focused on its role in global energy metabolism. Here, we performed mass-spectrometry-based global metabolite profiling in both cell extracts and culture media after MLN4924 treatment. While MLN4924 caused a general suppression of overall cellular metabolism including the TCA cycle, it increased glycolysis (Figure 4). Detailed mitochondrial functional assays revealed that MLN4924 impairs multiple mitochondrial functions, but increased mtDNA copy number and mitochondrial respiration (OXPHOS) (Figure 5), which is consistent with a recent study reporting that mitochondrial fusion was associated with enhanced cellular oxygen consumption, which required increased mtDNA to meet this functional change (45). MLN4924 also decreased overall cellular ATP content despite increased OXPHOS with increased ROS generation (Figure 5), consistent with a previous report that linked enhanced mitochondrial fusion to decreased mitochondrial ATP production (46). Collectively, our data suggest that impaired mitochondrial function with lower energy-generating efficiency is not fully compensated by an increased OXPHOS and glycolysis. Finally, our MFN1-knockdown-based rescue experiments revealed that MFN1 is responsible for MLN4924-induced fission-to-fusion conversion, partially responsible for altered mitochondrial functions, but had no effect on altered glycolysis.

The metabolic shift from decreased mitochondrial functions to increased glycolysis has been adopted by cancer cells to cope with metabolic need (12), termed the Warburg effect (11, 14). Here, we made the unexpected observation that neddylation blockage can induce this Warburg phenotype (Figure 6). Mechanistically, we focused on PKM2, a key enzyme whose activation is known to promote glycolysis (12, 13). We found that MLN4924-induced PK activity is solely due to PKM2 activation. We also showed that PKM2 activation by MLN4924 is not due to increased protein level, but due to induced formation of the tetrameric form, which was reported as the most active form of the enzyme (12). Our in vitro PKM2 activity assay further confirmed MLN4924 activation of PKM2, which is to an extent slightly more efficient than SAICAR, likely through binding that induces tetramer formation, given that MLN4924 and SAICAR have similar structures (36). Biologically, PKM2 knockdown sensitized breast cancer cells to MLN4924, further supporting an important role of PKM2 in cell growth (13), and indicating that PKM2 activation confers survival as a cellular protective mechanism against MLN4924 cytotoxicity.

Targeting global neddylation by its inhibitor MLN4924 has been demonstrated as an attractive anticancer strategy and MLN4924 has advanced into phase I/II clinical trials as a single agent or in combination with other anticancer drugs (15). We show that MLN4924 triggers mitochondrial fission-to-fusion conversion and increases OXPHOS and glycolysis, all of which confer survival to cancer cells. We therefore tested the therapeutic applicability of MLN4924 combined with either metformin or shikonin. Indeed, in both in vitro cell culture and 2 in vivo xenograft models, we found that the combination achieved much better growth suppression of cancer cells and xenograft tumors, as compared with single-agent treatment (Figure 7). Several recent cases have demonstrated anticancer efficacy by targeting metabolic reprogramming, such as in pancreatic cancer (47) and in acute myelogenous leukemia (23). It is worth noting that MLN4924 coupled with 2-deoxy-D-glucose, a glycolytic inhibitor (48), had much better efficacy in inducing cytotoxicity in breast cancer cells (49), as well as sensitized breast cancer cells to radiotherapy (50). Collectively, these preclinical studies together with our combination therapies (MLN4924/metformin and MLN4924/shikonin) could provide new avenues for the clinical combined use of MLN4924 for enhanced anticancer efficacy.

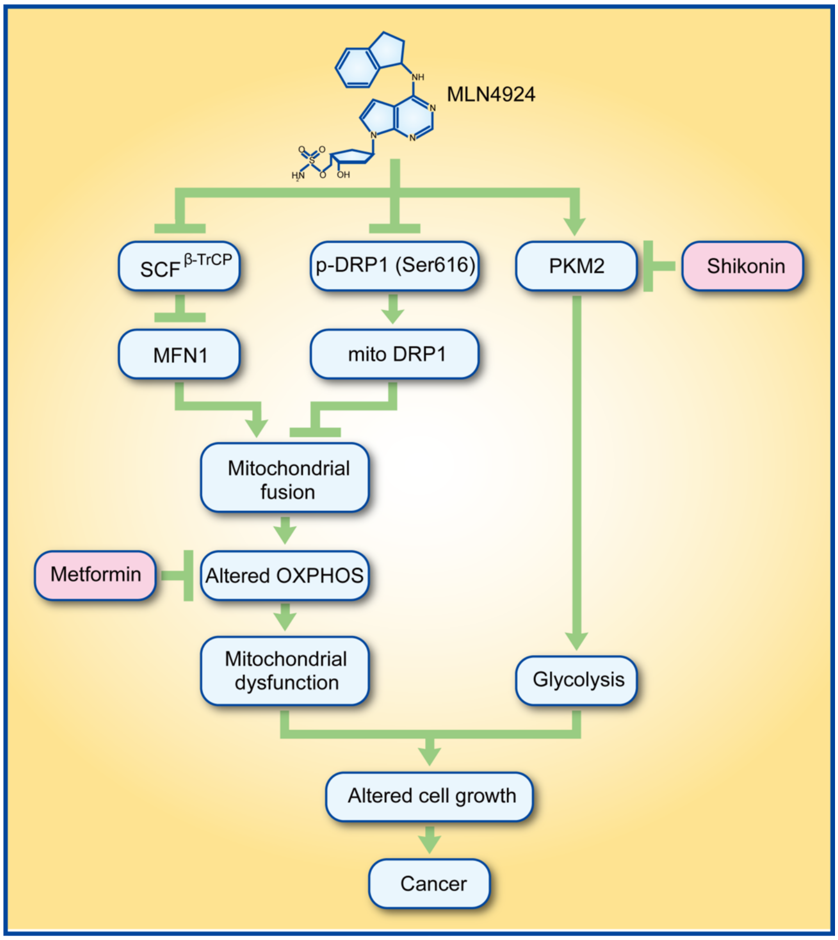

Figure 8. A working model. MLN4924, on one hand, inhibits mitochondrial functions and alters OXPHOS, and on the other hand, promotes glycolysis by activating PKM2. Combination of MLN4924 with the OXPHOS inhibitor metformin or the PKM2 inhibitor shikonin caused maximal suppression of breast cancer cell growth (see text for details).

In summary, we made 2 major findings in this study: (a) blockage of global neddylation altered energy metabolism with enhanced OXPHOS and glycolysis, but reduced mitochondrial functions; and (b) targeting OXPHOS and glycolysis significantly sensitizes breast cancer cells to MLN4924. Specifically, MLN4924, on one hand, alters mitochondrial functions by inducing mitochondrial fission-to-fusion conversion via inactivating $\mathrm{SCF}^{\beta\text{-TrCP}}$ E3 to cause MFN1 accumulation and via blocking DRP1 mitochondrial translocation; and on the other hand, promotes glycolysis by activating PKM2 via inducing tetrameric formation, eventually conferring protection to cancer cells. Targeted combination of MLN4924 with metformin or shikonin abrogates these cellular protective mechanisms, leading to enhanced cancer cell killing (Figure 8). Our study, therefore, demonstrated that energy metabolism is subject to neddylation regulation, and also provides proof-of-concept evidence for rational drug combinations to increase efficacy of cancer therapy.

Methods

Cell culture and transfection. Human breast cancer lines MDA-MB-231 and SK-BR-3, lung cancer cell lines A549, H1299, and H1650, lung bronchial epithelial cell line BEAS2B, embryonic kidney cell line HEK293, and cervical cancer cell line HeLa were obtained from American Type Culture Collection. MDA-MB-231, H1650, and BEAS2B cells were cultured in RPMI 1640 medium (Invitrogen), whereas SK-BR-3, H1299, A549, HEK293, and HeLa cells were cultured in DMEM (Invitrogen), supplemented with 10% FBS (Gibco) and incubated at 5% CO_2, 37°C, and 95% humidity.

Cells were transfected with various plasmids using Lipofectamine 3000 Transfection Reagent or with si-RNA oligonucleotides by Lipofectamine RNAiMAX Transfection Reagent, according to the manufacturer's instructions (see below).

Antibodies and reagents. The following antibodies were used: CUL-1 (Santa Cruz Biotechnology, sc-11384); MFN1 (Abnova, M04, clone 3C9); MFN2 (Abnova, M03, clone 4H8); DRP1 (Nonus, NB110-55237); phospho-DRP1 (Ser616) (Cell Signaling Technology, 3455S); Tom20 (Proteintech, 11802-1-AP); RBX1 (Cell Signaling Technology, 11922S); Parkin (Cell Signaling Technology, 4211S); HA (Sigma-Aldrich, H6908); FLAG (Sigma-Aldrich, F7425-2MG); monoclonal anti–FLAG M2, clone M2 (Sigma-Aldrich, F1804-500UG), anti–FLAG M2 affinity gel (Sigma-Aldrich, A2220-5ML); monoclonal anti-HA-Agarose antibody (Sigma-Aldrich, A2095-1ML); NAEβ (Abcam, ab124728); β-TrCP1 (Cell Signaling Technology, 4394S); PKM2 (Cell Signaling Technology, 4053S); PKM1 (Cell Signaling Technology, 7067S); β-actin (Sigma-Aldrich, A5441); α-tubulin (Sigma-Aldrich, clone AA13, T8203); Alexa Fluor 488 donkey anti-rabbit IgG (H+L) (Life Technologies, A-21206); goat anti-mouse IgG-HRP (Santa Cruz Biotechnology, sc-2005); and goat anti-rabbit IgG-HRP (Santa Cruz Biotechnology, sc-2004).

Reagents were obtained from the following suppliers: MLN4924 (ApexBio, B1036), as well as a gift from Takeda Pharmaceuticals, Inc; chlorhexidine (CHX) (Sigma-Aldrich, C7698); MitoTracker Red (Life Technologies, M7512); metformin (Sigma-Aldrich, LRAA1730); shikonin (Selleck, S8279); SAICAR (Cayman Chemical, 14087); MG132 (MedChem Express, HY-13259); Ni-NTA Agarose (Qiagen, 30210); Lipofectamine RNAiMAX Transfection Reagent (Invitrogen, 13778-150); Lipofectamine 3000 Transfection Reagent (Invitrogen, L3000-015); and DAPI (Roche, 237276).

Plasmids and siRNAs. Mito-DS-Red was from Stephen L. Archer (Queen's University, Kingston, Ontario, Canada), HA-DRP1 was from Craig Blackstone (NIH, Bethesda, Maryland, USA) and pCold I PKM2 was from Zhimin Lu (University of Texas MD Anderson Cancer Center, Houston, Texas, USA). si-RNAs were synthesized by RiboBio. The sequences of si-RNAs are as follows: MFN1-1, 5′-AAGGGGAUUACUGCAAUCUUUdTdT-3′; MFN1-2, 5′-CCAAGGAGCGAGCCUUUAAdTdT-3′; MFN2-1, 5′-AAGAGACACAUGGCUGAGGUGdTdT-3′; MFN2-2, 5′-CCAGUAGUCCUCAAGGUUUdTdT-3′ (51); NAEβ-1, 5′-GCUUCUCUGCAAAUGAAAUdTdT-3′; NAEβ-2, 5′-GCUACCAGAACACUGTAUUdTdT-3′; TrCP, 5′-AAGUGGAAUUUGUGGAACAUCdTdT-3′; PKM2-1, 5′-AGGCAGAGGCUGCCAUCUAdTdT-3′; and PKM2-2, 5′-CCAUAAUCGUCCUCACCAAdTdT-3′ (52).

Immunostaining and confocal microscopy. Cells grown on coverslips were fixed with 4% paraformaldehyde solution for 10 minutes. The coverslips were washed 3 times with PBS and incubated in PBS, pH 7.4, containing 10% FBS to block nonspecific sites of antibody adsorption. Cells were then incubated with appropriate primary and secondary antibodies in 0.1% saponin. For mitochondrial staining, cells were incubated with 60 nM MitoTracker Red for 30 minutes at 37°C. Images were captured on a confocal microscope (FV1000, Olympus).

Electron microscopy. Cells were fixed with 2.5% glutaraldehyde overnight at 4°C. After washing in 100 mM phosphate buffer (pH 7.4), cells were postfixed for 1.5 hours at room temperature in 1% osmium tetroxide, followed by washing with phosphate buffer, dehydrated in 30%, 50%, 70%, 80%, 95%, and 100% ethanol and then 100% acetone. The samples were then infiltrated sequentially in 1:1 (vol/vol) acetone/Spurr resin (Sigma-Aldrich) for 1 hours, 1:3 acetone/Spurr resin for 3 hours, and finally 100% Spurr resin for 24 hours and polymerized for another 24 hours at 65°C. Sections were imaged with a Tecnai G2 Spirit 120 kV transmission electron microscope (FEI Company).

Immunoblots and immunoprecipitation. For direct immunoblot analysis, proteins from lysed cells were quantified with the Bio-Rad protein assay kit (catalog 500-0002EDU). The denatured proteins were resolved by SDS-PAGE, transferred to PVDF membranes, and followed with immunoblot analysis with various antibodies. See complete unedited blots in the supplemental material.

For immunoprecipitation analysis, transfected cell lysates were incubated with bead-conjugated Flag or HA in a rotating incubator overnight at 4°C. The immunoprecipitates were washed with lysis buffer and detected by immunoblot analysis.

Protein half-life measurement. Cells were transfected with indicated plasmids or siRNA against MFN1 for 48 hours, then treated with 50 μg/ml CHX for various time points and collected for immunoblotting. The band density was quantified using ImageJ software (NIH).

In vivo ubiquitylation assay. HEK293 cells were transfected with constructs encoding β-TrCP1, HA-his-Ub, MFN1, or MFN1 S85/86/90A mutant, along with empty construct or β-TrCP1ΔF controls. Forty-eight hours after transfection, cells were treated with MG132 (20 μM) for 6 hours and then lysed with denatured buffer containing 6 M guanidine as described previously (53). MFN1-ploy-Ub was purified by Ni-bead pulldown and detected by immunoblot using MFN1 antibody.

Flow cytometry. Cells were harvested and fixed with 75% ethanol overnight, then washed twice with PBS and suspended in PI/RNase Staining Buffer (BD Pharmingen) for 15 minutes in the dark. The samples were analyzed using an FC500 MPL flow cytometer (Beckman Coulter) for cell cycle distribution.

Cell viability and clonogenic survival assays. Cells were harvested, suspended in PBS, and mixed with 0.4% solution of trypan blue (Sigma-Aldrich). Viable cells were counted. For clonogenic survival assay, 500 cells were seeded in 3-cm dishes, followed by incubation for 10 days with drug-containing fresh medium. The colonies were fixed, stained, and counted under an inverted microscope. Colonies with 50 cells or more were counted.

Metabolic profiling analysis. The untargeted metabolic profiling analysis was performed on the XporeMET platform (Metabo-Profile) and sample preparation was performed as previously described (54).

Mitochondria isolation. A cell mitochondria isolation kit was purchased from Beyotime (C3601) and the assay was performed according to the manufacturer's instructions.

Measurement of mitochondrial membrane potential. Mitochondrial membrane potential was assessed with a Mitochondria Staining Kit (JC-1) (MultiSciences, 125T). In brief, cells were collected in staining buffer and JC-1 was added for 30 minutes at 37°C and 5% CO_2. Alternatively, cells were preincubated with protonophore uncoupler carbonyl cyanide 3-chlorophenylhydrazone (CCCP) for 5 minutes at 37°C and 5% CO_2 prior to staining with JC-1. Sample fluorescence was measured by flow cytometry.

Measurement of intracellular ATP levels. The ATP levels in cells were measured using an ATP-lite Luminescence Assay Kit (PerkinElmer) according to the manufacturer's protocol and ATP levels were normalized to protein content.

Detection of mitochondrial copy number. Total cellular DNA was isolated using the Genomic DNA Extraction Kit (Takara, 9765). Quantitative real-time RT-PCR assay was used to detect the mtDNA number. mtDNA levels were detected using primers for mtDNA-encoded human gene 16S rRNA (5′-GCACACCCGTCTATGTAGCAAA-3′ and 5′-GATTTAGAGGGTTCTGTGGGCA-3′), and nuclear DNA levels was detected using primers for human β-globin (5′-AGAAACTGGGCATGTGGAGACA-3′ and 5′-ATGAGCCTTCACCTTAGGGTTG-3′). mtDNA was normalized to nuclear DNA.

Measurement of mitochondrial ROS. ROS generation by mitochondria in living cells was analyzed using the mitochondrial superoxide indicator Mitosox Red (Invitrogen, M36008). Samples were analyzed by flow cytometry with excitation at 510 nm and emission at 580 nm.

Measurement of OCR and ECAR. OCR and ECAR were measured using the XF96 Analyzer (Seahorse Bioscience). Briefly, cells were seeded in 96-well FluxPaKs (Seahorse Bioscience) and treated with various concentrations of MLN4924 for the indicated time periods. Before running the Seahorse assay, cells were incubated for 30 minutes in unbuffered DMEM without CO_2. OCR and ECAR were detected simultaneously under basal conditions and after the sequential addition of oligomycin (1 μM), fluro-carbonyl cyanide phenylhydrazone (FCCP) (0.5 μM), rotenone (1 μM), and antimycin A (5 μM). After measurement of OCR and ECAR, data were normalized to the cell number in each well.

Measurement of glucose metabolism. Cells were seeded onto culture dishes and treated with various concentrations of MLN4924 for the indicated time periods. The media were then collected to measure the concentration of glucose, pyruvate, and lactate. Glucose levels were detected using a glucose assay kit (Shanghai Rongsheng Biotech). Glucose consumption was calculated by deducting the remaining glucose in the medium from the original glucose in the media. Pyruvate and lactate production was measured using a pyruvate assay kit and lactate assay kit (Nanjing Jiancheng Bioengineering Institute). Pyruvate kinase activity was detected using a pyruvate kinase kit (Solarbio, BC0545). All values were normalized according to cell number.

In vitro PKM2 activity assay. Briefly, pCold I PKM2 was transformed into BL21 Codonplus RIL (DE3) cells. PKM2 expression was induced by IPTG and cell pellets were suspended in lysis buffer (50 mM NaH_2PO_4, 300 mM NaCl, 10 mM imidazole, pH 7.4) supplemented with protease inhibitor cocktail. Cells were lysed by sonication, and cell debris was removed by centrifugation. Supernatant was incubated with Ni-NTA agarose (Qiagen) for 4 hours at 4°C. PKM2 protein was recovered by centrifugation, eluted with elution buffer (50 mM NaH_2PO_4, 300 mM NaCl, 250 mM imidazole, pH 7.4), and the purity was verified by PAGE. The in vitro pyruvate kinase activity was measured using a pyruvate kinase kit (Solarbio, BC0545) and 2.5 μM PKM2 (elution fractions 1 and 2) was used alone or with different concentrations of MLN4924 or SAICAR.

Crosslinking assay. Cells were treated with various concentrations of MLN4924 for 24 hours, and then trypsinized and counted. Equal numbers of cells were collected for experiments. The whole-cell lysates were crosslinked with 0.025% glutaraldehyde for 3 minutes at 37°C and terminated with Tris-HCl (pH 8.0, 1 M), followed by Western blotting with the indicated antibodies.

In vivo tumorigenesis assay. MDA-MB-231 cells (1×10^6) or SK-BR3 cells (3×10^6) in 100 μl PBS were mixed with 100 μl Matrigel (Corning) and inoculated subcutaneously in both franks into female SCID mice (7–8 weeks old) (from Charles River) or nude mice (7–8 weeks old) (Jackson Laboratories, stock number 007850), respectively. When the tumor size reached approximately 100 mm^3 at about 14 days after inoculation, the mice were randomized and treated for 21 days (MDA-MB-231 model) or 18 days (SK-BR-3 model). MLN4924 (30 mg/kg) or vehicle solution (10% hydroxypropyl β-cyclodextrin) was given to mice by subcutaneous injection, 5 days a week, and metformin (200 mg/kg) and shikonin (1 mg/kg) were given to mice via intraperitoneal injection, 5 days and 2 days a week, respectively. Tumor size and body weight were monitored twice a week for 3 weeks, and average tumor volumes were calculated as estimated from the formula $(L \times W^2)/2$. At the end of experiment, tumors were harvested and weighed.

Statistics. All experiments were repeated at least 3 independent times and the representative data are presented as mean ± standard deviation (SD). A linear mixed-effects model was used to compare tumor growth rates among the control and treatment groups based on log-transformed tumor volumes measured over time. The model includes a random intercept and a random slope so that each tumor has its own growth profile. The fit of the model was visually checked by various residual plots. Additionally, we compared tumor volume doubling times among each group. Tumor volume doubling was determined for each xenograft by identifying the earliest day on which it was at least twice as large as on the first day of treatment. A cubic smoothing spline was used to obtain the exact time of doubling. Then the doubling times were estimated using Kaplan-Meier methods and compared among the groups using log-rank tests to generate survival probability. One-way or 2-way analysis of variance (ANOVA) was performed to determine the significance among the groups. Among all the data sets, P values less than 0.05 were considered significant and are denoted as $^*P < 0.05$, $^{**}P < 0.01$.

Study approval. All animal studies were approved by and conducted in accordance with the guidelines established by the Committee on Use and Care of Animals at the University of Michigan (UM approval number RPO00006919).

Author contributions

QZ and YS conceived and designed the research, and QZ performed most of the experiments. HL, MT, and SF performed animal experiments. YL performed some experiments on glycolysis. L. Zhao analyzed animal data. Oxygen consumption experiments were performed in the Guan laboratory with the assistance of CC, FM, L. Zhu, and MXG. HJ provided glycolytic reagents and partial funding. QZ and YS wrote the manuscript.

Acknowledgments

We would like to thank Qingfeng Yan and Pingping Jiang for their support in measurement of mitochondrial DNA copy number and oxygen consumption rate, respectively. We would also like to thank the staff members at the Core facilities and the Center of Cryo Electron Microscopy at the Zhejiang University School of Medicine for their assistance in confocal microscopy, flow cytometry analyses, and transmission electron microscopy. We also thank Zhimin Lu for providing us with the PKM2 plasmid and Takeda Pharmaceutical for providing us with MLN4924. This work is supported in part by the National Key R&D Program of China (2016YFA0501800 to YS); Chinese NSFC grants 31701167 (to QZ) and 81572718 (to YS); Natural Science Foundation of Zhejiang Province grant LY17C070001 (to QZ); Zhejiang Medical Technology and Education grants 2017180631 and 2018249124 (to QZ), Fundamental Research Funds for the Central Universities 2018FZA7005 (to QZ); and NCI grants CA156744 and CA171277 (to YS). YS also gratefully acknowledges the support of the K.C. Wong Education Fund.

Address correspondence to: Yi Sun, University of Michigan, 4424B MS-1, 1301 Catherine Street, Ann Arbor, Michigan 48109, USA. Phone: 734.615.1989; Email: sunyi@umich.edu or yisun@zju.edu.cn.

---

1. Wallace DC, Fan W. Energetics, epigenetics, mitochondrial genetics. *Mitochondrion*. 2010;10(1):12–31.
2. Wallace DC. Mitochondria and cancer. *Nat Rev Cancer*. 2012;12(10):685–698.
3. Hanahan D, Weinberg RA. Hallmarks of cancer: the next generation. *Cell*. 2011;144(5):646–674.
4. Gonsalves WI, et al. Glutamine-derived 2-hydroxyglutarate is associated with disease progression in plasma cell malignancies. *JCI Insight*. 2018;3(1):e94543.
5. Vander Heiden MG, DeBerardinis RJ. Understanding the intersections between metabolism and cancer biology. *Cell*.

2017;168(4):657–669.

6. Siska PJ, et al. Mitochondrial dysregulation and glycolytic insufficiency functionally impair CD8 T cells infiltrating human renal cell carcinoma. *JCI Insight*. 2017;2(12):e93411.
7. Porporato PE, Filigheddu N, Pedro JMB, Kroemer G, Galluzzi L. Mitochondrial metabolism and cancer. *Cell Res*. 2018;28(3):265–280.
8. Mishra P, Chan DC. Mitochondrial dynamics and inheritance during cell division, development and disease. *Nat Rev Mol Cell Biol*. 2014;15(10):634–646.
9. Mishra P, Chan DC. Metabolic regulation of mitochondrial dynamics. *J Cell Biol*. 2016;212(4):379–387.
10. Senft D, Ronai ZA. Regulators of mitochondrial dynamics in cancer. *Curr Opin Cell Biol*. 2016;39:43–52.
11. Warburg O. On the origin of cancer cells. *Science*. 1956;123(3191):309–314.
12. Dayton TL, Jacks T, Vander Heiden MG. PKM2, cancer metabolism, and the road ahead. *EMBO Rep*. 2016;17(12):1721–1730.
13. Chen J, Xie J, Jiang Z, Wang B, Wang Y, Hu X. Shikonin and its analogs inhibit cancer cell glycolysis by targeting tumor pyruvate kinase-M2. *Oncogene*. 2011;30(42):4297–4306.
14. Lévy P, Bartosch B. Metabolic reprogramming: a hallmark of viral oncogenesis. *Oncogene*. 2016;35(32):4155–4164.
15. Zhou L, Zhang W, Sun Y, Jia L. Protein neddylation and its alterations in human cancers for targeted therapy. *Cell Signal*. 2018;44:92–102.
16. Zhao Y, Sun Y. Cullin-RING ligases as attractive anti-cancer targets. *Curr Pharm Des*. 2013;19(18):3215–3225.
17. Wang Z, Liu P, Inuzuka H, Wei W. Roles of F-box proteins in cancer. *Nat Rev Cancer*. 2014;14(4):233–247.
18. Soucy TA, et al. An inhibitor of NEDD8-activating enzyme as a new approach to treat cancer. *Nature*. 2009;458(7239):732–736.
19. Zhang Q, Karnak D, Tan M, Lawrence TS, Morgan MA, Sun Y. FBXW7 facilitates nonhomologous end-joining via K63-linked polyubiquitylation of XRCC4. *Mol Cell*. 2016;61(3):419–433.
20. Zhao Y, Xiong X, Jia L, Sun Y. Targeting Cullin-RING ligases by MLN4924 induces autophagy via modulating the HIF1-REDD1-TSC1-mTORC1-DEPTOR axis. *Cell Death Dis*. 2012;3:e386.
21. Swords RT, et al. Inhibition of NEDD8-activating enzyme: a novel approach for the treatment of acute myeloid leukemia. *Blood*. 2010;115(18):3796–3800.
22. Luo Z, et al. The Nedd8-activating enzyme inhibitor MLN4924 induces autophagy and apoptosis to suppress liver cancer cell growth. *Cancer Res*. 2012;72(13):3360–3371.
23. Nawrocki ST, et al. The NEDD8-activating enzyme inhibitor MLN4924 disrupts nucleotide metabolism and augments the efficacy of cytarabine. *Clin Cancer Res*. 2015;21(2):439–447.
24. Rehman J, et al. Inhibition of mitochondrial fission prevents cell cycle progression in lung cancer. *FASEB J*. 2012;26(5):2175–2186.
25. Zhao Y, Morgan MA, Sun Y. Targeting Neddylation pathways to inactivate cullin-RING ligases for anticancer therapy. *Antioxid Redox Signal*. 2014;21(17):2383–2400.
26. Brownell JE, et al. Substrate-assisted inhibition of ubiquitin-like protein-activating enzymes: the NEDD8 E1 inhibitor MLN4924 forms a NEDD8-AMP mimetic in situ. *Mol Cell*. 2010;37(1):102–111.
27. Chen H, Detmer SA, Ewald AJ, Griffin EE, Fraser SE, Chan DC. Mitofusins Mfn1 and Mfn2 coordinately regulate mitochondrial fusion and are essential for embryonic development. *J Cell Biol*. 2003;160(2):189–200.
28. Smirnova E, Griparic L, Shurland DL, van der Bliek AM. Dynamin-related protein Drp1 is required for mitochondrial division in mammalian cells. *Mol Biol Cell*. 2001;12(8):2245–2256.
29. Zhang L, et al. Altered brain energetics induces mitochondrial fission arrest in Alzheimer's disease. *Sci Rep*. 2016;6:18725.
30. Westrate LM, Sayfie AD, Burgenske DM, MacKeigan JP. Persistent mitochondrial hyperfusion promotes G2/M accumulation and caspase-dependent cell death. *PLoS One*. 2014;9(3):e91911.
31. Yang D, Tan M, Wang G, Sun Y. The p21-dependent radiosensitization of human breast cancer cells by MLN4924, an investigational inhibitor of NEDD8 activating enzyme. *PLoS One*. 2012;7(3):e34079.
32. Gegg ME, Cooper JM, Chau KY, Rojo M, Schapira AH, Taanman JW. Mitofusin 1 and mitofusin 2 are ubiquitinated in a PINK1/parkin-dependent manner upon induction of mitophagy. *Hum Mol Genet*. 2010;19(24):4861–4870.
33. Choo YS, et al. Regulation of parkin and PINK1 by neddylation. *Hum Mol Genet*. 2012;21(11):2514–2523.
34. Denison SR, et al. Alterations in the common fragile site gene Parkin in ovarian and other cancers. *Oncogene*. 2003;22(51):8370–8378.
35. Lin HY, et al. Suppressor of cytokine signaling 6 (SOCS6) promotes mitochondrial fission via regulating DRP1 translocation. *Cell Death Differ*. 2013;20(1):139–153.
36. Keller KE, Tan IS, Lee YS. SAICAR stimulates pyruvate kinase isoform M2 and promotes cancer cell survival in glucose-limited conditions. *Science*. 2012;338(6110):1069–1072.
37. Wheaton WW, et al. Metformin inhibits mitochondrial complex I of cancer cells to reduce tumorigenesis. *Elife*. 2014;3:e02242.
38. Vander Heiden MG. Targeting cancer metabolism: a therapeutic window opens. *Nat Rev Drug Discov*. 2011;10(9):671–684.
39. Pagliuso A, et al. A role for septin 2 in Drp1-mediated mitochondrial fission. *EMBO Rep*. 2016;17(6):858–873.
40. Trotta AP, Chipuk JE. Mitochondrial dynamics as regulators of cancer biology. *Cell Mol Life Sci*. 2017;74(11):1999–2017.
41. Cohen MM, Leboucher GP, Livnat-Levanon N, Glickman MH, Weissman AM. Ubiquitin-proteasome-dependent degradation of a mitofusin, a critical regulator of mitochondrial fusion. *Mol Biol Cell*. 2008;19(6):2457–2464.
42. Park YY, Lee S, Karbowski M, Neutzner A, Youle RJ, Cho H. Loss of MARCH5 mitochondrial E3 ubiquitin ligase induces cellular senescence through dynamin-related protein 1 and mitofusin 1. *J Cell Sci*. 2010;123(Pt 4):619–626.
43. Bonnen PE, et al. Mutations in FBXL4 cause mitochondrial encephalopathy and a disorder of mitochondrial DNA maintenance. *Am J Hum Genet*. 2013;93(3):471–481.
44. Liu Y, et al. The proapoptotic F-box protein Fbxl7 regulates mitochondrial function by mediating the ubiquitylation and proteasomal degradation of survivin. *J Biol Chem*. 2015;290(19):11843–11852.
45. Reznik E, et al. Mitochondrial DNA copy number variation across human cancers. *Elife*. 2016;e10769.
46. Grandemange S, Herzig S, Martinou JC. Mitochondrial dynamics and cancer. *Semin Cancer Biol*. 2009;19(1):50–56.
47. Franco J, Balaji U, Freinkman E, Witkiewicz AK, Knudsen ES. Metabolic reprogramming of pancreatic cancer mediated by CDK4/6 inhibition elicits unique vulnerabilities. *Cell Rep*. 2016;14(5):979–990.
48. Zhou Q, et al. Mechanistic study on the nuclear modifier gene MSS1 mutation suppressing neomycin sensitivity of the mitochondrial

15S rRNA C1477G mutation in Saccharomyces cerevisiae. *PLoS One*. 2014;9(3):e90336.

49. Oladghaffari M, et al. High efficiency apoptosis induction in breast cancer cell lines by MLN4924/2DG co-treatment. *Asian Pac J Cancer Prev*. 2015;16(13):5471–5476.
50. Oladghaffari M, et al. MLN4924 and 2DG combined treatment enhances the efficiency of radiotherapy in breast cancer cells. *Int J Radiat Biol*. 2017;93(6):590–599.
51. Sugioka R, Shimizu S, Tsujimoto Y. Fzo1, a protein involved in mitochondrial fusion, inhibits apoptosis. *J Biol Chem*. 2004;279(50):52726–52734.
52. Goldberg MS, Sharp PA. Pyruvate kinase M2-specific siRNA induces apoptosis and tumor regression. *J Exp Med*. 2012;209(2):217–224.
53. Xu J, et al. The β-TrCP-FBXW2-SKP2 axis regulates lung cancer cell growth with FBXW2 acting as a tumour suppressor. *Nat Commun*. 2017;8:14002.
54. Ni Y, et al. ADAP-GC 2.0: deconvolution of coeluting metabolites from GC/TOF-MS data for metabolomics studies. *Anal Chem*. 2012;84(15):6619–6629.